Cell Reports

Article

VIP-expressing interneurons in the anterior insular cortex contribute to sensory processing to regulate adaptive behavior

Graphical abstract

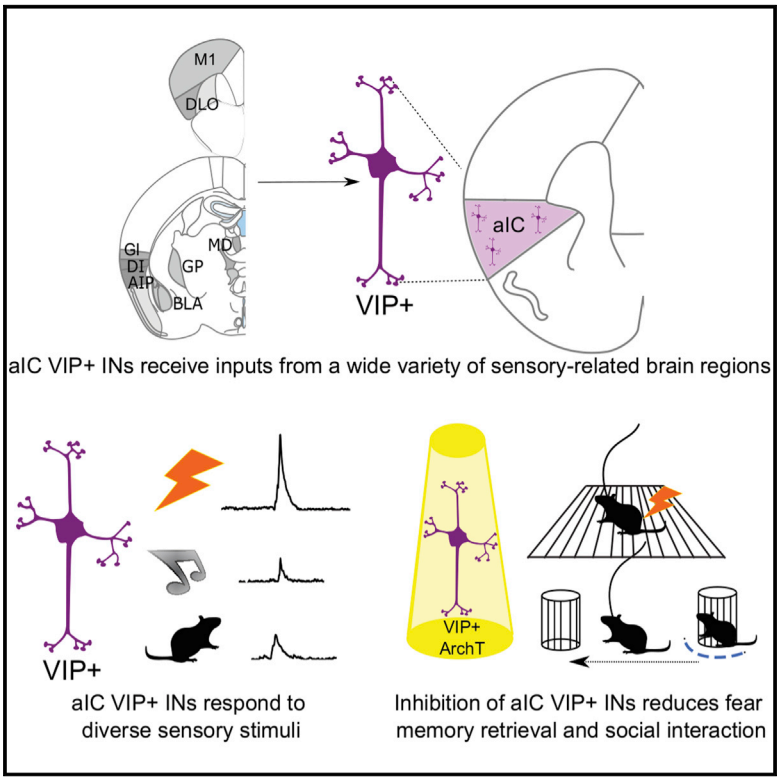

Authors

Arnau Ramos-Prats, Enrica Paradiso, Federico Castaldi, ..., Heide Hörtnagl, Georg Göbel, Francesco Ferraguti

Correspondence

francesco.ferraguti@i-med.ac.at

In brief

The mechanisms underlying the responses of specific subclasses of interneurons to sensory stimuli with potential importance for behavioral adaptations is largely unknown. Ramos-Prats et al. identify VIP+ interneurons (INs) in the anterior insular cortex (aIC) as mediators of sensory processing and adaptive behaviors, such as social preference and fear learning.

Highlights

- aIC VIP+ INs receive inputs from a wide variety of sensory-related brain regions
- aIC VIP+ INs respond to diverse sensory stimuli
- Inhibition of aIC VIP+ INs reduces fear memory retrieval and social interaction
- aIC VIP+ INs are functionally heterogeneous and display coding instability

Ramos-Prats et al., 2022, Cell Reports *39*, 110893
May 31, 2022
https://doi.org/10.1016/j.celrep.2022.110893

CellPress

Cell Reports

CellPress
OPEN ACCESS

Article

VIP-expressing interneurons in the anterior insular cortex contribute to sensory processing to regulate adaptive behavior

Arnau Ramos-Prats,[1] Enrica Paradiso,[1] Federico Castaldi,[1] Maryam Sadeghi,[2] Mohd Yaqub Mir,[1,3] Heide Hörtnagl,[1] Georg Göbel,[2] and Francesco Ferraguti[1,4,*]

[1]Department of Pharmacology, Medical University of Innsbruck, 6020 Innsbruck, Austria
[2]Department for Medical Statistics, Informatics and Health Economics, Medical University of Innsbruck, 6020 Innsbruck, Austria
[3]Szentágothai Doctoral School of Neuroscience, Semmelweis University, 1121 Budapest, Hungary
[4]Lead contact
*Correspondence: francesco.ferraguti@i-med.ac.at
https://doi.org/10.1016/j.celrep.2022.110893

SUMMARY

Adaptive behavior critically depends on the detection of behaviorally relevant stimuli. The anterior insular cortex (aIC) has long been proposed as a key player in the representation and integration of sensory stimuli, and implicated in a wide variety of cognitive and emotional functions. However, to date, little is known about the contribution of aIC interneurons to sensory processing. By using a combination of whole-brain connectivity tracing, imaging of neural calcium dynamics, and optogenetic modulation in freely moving mice across different experimental paradigms, such as fear conditioning and social preference, we describe here a role for aIC vasoactive intestinal polypeptide-expressing (VIP+) interneurons in mediating adaptive behaviors. Our findings enlighten the contribution of aIC VIP+ interneurons to sensory processing, showing that they are anatomically connected to a wide range of sensory-related brain areas and critically respond to behaviorally relevant stimuli independent of task and modality.

INTRODUCTION

One of the evolutionary advantages associated with the development of complex cortical circuitry is the ability to discriminate specific stimuli from a stream of ascending sensory information and to adapt to their repeated presentation to enable flexible behavioral responses. Behavioral relevance is attributed based on previous experiences, temporary need state, and disposition of an organism, which requires associative, emotional, and/or cognitive learning processes (Downar et al., 2001, 2002; Corbetta et al., 2008). The insular cortex, and in particular its anterior part (aIC), has been linked to adaptive behavioral functions, including aversive state processing (Gehrlach et al., 2019; Gogolla, 2017; Livneh and Andermann, 2021) and social interactions (Lamm and Singer, 2010; Miura et al., 2020).

Within cortical circuits, specific interneuron (IN) subtypes are recruited with reference to a given network state or behavioral contingency (Letzkus et al., 2011; Pakan et al., 2016; Kuchibhotla et al., 2017; Turi et al., 2019). By refining the response properties of principal neurons, INs control cortical excitability and are hypothesized to contribute to behavioral state-dependent modulation of sensory processing (Krabbe et al., 2018; Kvitsiani et al., 2013; Kim et al., 2016; Lee et al., 2019; Fu et al., 2014). However, little is known about the mechanisms underlying the responses of specific subclasses of aIC INs to sensory stimuli with potential importance for behavioral adaptations. In cortical circuits, VIP+ INs comprise a major, but heterogeneous, class of GABAergic neurons (Guet-Mccreight et al., 2020; Porter et al., 1998; Prönneke et al., 2015; Rhomberg et al., 2018). In the neocortex as well as basolateral amygdala (BLA), VIP+ INs are highly active during states of arousal and are modulated by context-dependent behaviors and reinforcement learning (Krabbe et al., 2019; Pi et al., 2013; Kuchibhotla et al., 2017; Garrett et al., 2020; Kastli et al., 2020). These INs have been shown to provide disinhibitory control onto somatostatin- and parvalbumin-expressing INs gating the information flow onto downstream principal neurons (Krabbe et al., 2019; Pi et al., 2013; Guet-Mccreight et al., 2020; Walker et al., 2016).

Recent studies have suggested the importance of VIP+ INs in gain modulation to facilitate sensory discrimination (Batista-Brito et al., 2017; Ayzenshtat et al., 2016). Thus, we hypothesized that this specific subtype of IN is crucial for the processing of sensory stimuli in the aIC, an area that mediates complex adaptive behaviors, such as social preference (Miura et al., 2020) and associative learning (Shi et al., 2020; Lissek, 2012). To test this hypothesis, we used a combination of viral mono-trans-synaptic tracing and deep-brain Ca^{2+} imaging, as well as *in vivo* optogenetic manipulation of aIC VIP+ INs. We report that aIC VIP+ INs receive long-range inputs from a wide variety of sensory-related brain regions and are activated, both at the population and individual cell level, by sensory stimuli of different modalities. We further show that aIC VIP+ IN activity influences adaptive behaviors, such as fear

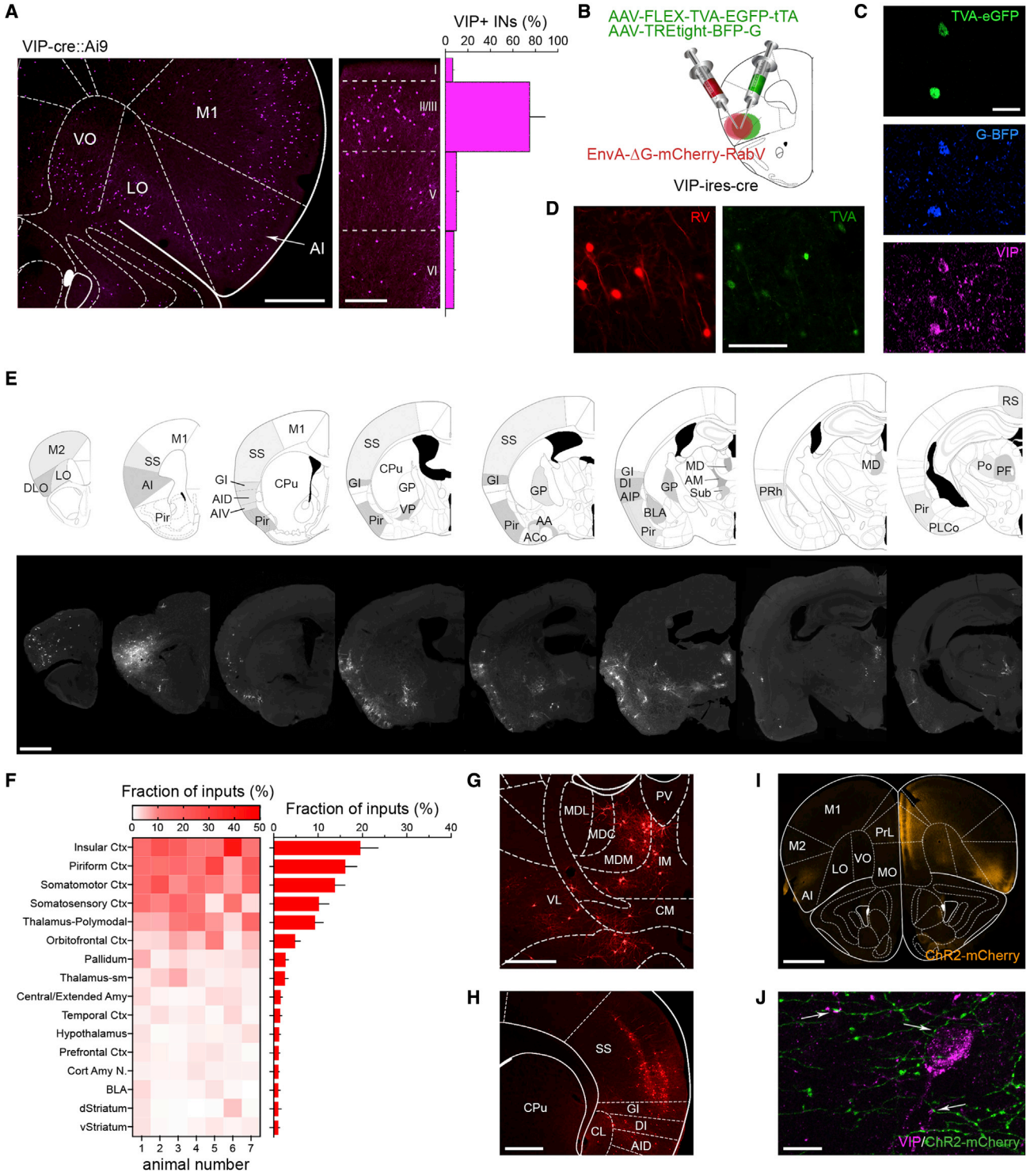

Figure 1. Distribution of VIP+ INs in the IC and first-order long-range presynaptic inputs

(A) Example images of VIP expression throughout the IC in a VIP-ires-cre:Ai9-tdTomato reporter mouse (left and middle panels) and immunohistochemical quantification of VIP+ INs throughout the different cortical layers of the aIC (right panel; N = 3 mice). Scale bars, 500 and 250 μm.

(B) Schematics of the mono-trans-synaptic retrograde tracing strategy employed to identify inputs to aIC VIP+ INs.

(C) Example images of TVA-EGFP-tTA, G-BFP, and VIP expression in aIC VIP+ INs. Scale bar, 20 μm.

(D) Example images of TVA-EGFP-tTA and mCherry-RabV (RV) expression in aIC VIP+ INs. Scale bar, 100 μm.

(legend continued on next page)

memory retrieval and social preference. Finally, we reveal that, although functionally different VIP+ INs exist, their coding specificity is flexible across days and behavioral paradigms.

RESULTS

Distribution of VIP+ INs in the IC and detection of their first-order long-range presynaptic inputs

At first, we have investigated the general distribution of VIP+ INs across different mouse insular cortex subdivisions and along its entire rostro-caudal axis, by means of immunohistochemistry (IHC), since it has never been expressly studied before. The highest percentage of VIP+ INs was found in cortical layer II/III (Figure 1A), similar to other neocortical regions (He et al., 2016; Mesik et al., 2015; Prönneke et al., 2015). The sensitivity of our VIP-IHC analysis was confirmed in transgenic VIP:Ai9-tdTomato mice, in which 99.7% of the VIP immunoreactive neurons co-expressed the reporter tdTomato (Figures S1A–S1D). Among all insular cortex subdivisions, the aIC and, in particular, the agranular component, showed the highest density (Figures S1E and S1F).

Next, to identify the main brain regions projecting to aIC VIP+ INs and potentially driving their activity, we used a viral monotrans-synaptic tracing approach (Liu et al., 2017; Lavin et al., 2020) that restricted the retrograde tracing from VIP+ INs only (Figures 1B–1D, S2A, and S2B). This approach revealed direct inputs from brain areas involved in the processing of sensory information (Figures 1E and 1F), such as the somatosensory (Figure 1H; 10.22%) and piriform cortex (Figure S2E; 16.5%). Moreover, a high percentage of inputs was identified in brain regions belonging to the salience network (SN) (Sforazzini et al., 2014; Seeley et al., 2007). These included areas of the insular cortex outside the injection site (19.5%) and the midline polymodal thalamic nuclei (9.3%), such as the mediodorsal thalamus (MD) (Figures 1G, S2C, and S2D), for which direct inputs to aIC VIP+ INs were further confirmed by anterograde tracing (Figures 1I, 1J, S2F-2I). Additional areas with a significant number of presynaptic neurons were the orbitofrontal cortex (4.8%), the basal forebrain (Figure S2E; 2.7%), which includes the ventral pallidum known to drive the activity of cortical INs (Lin and Nicolelis, 2008; Hangya et al., 2015), and the basolateral amygdala (Figure S2E; 1.1%).

aIC VIP+ INs are activated in response to different tasks and sensory stimuli

To reveal the activity of aIC VIP+ INs at single-cell resolution in response to stimuli of diverse sensory modalities during different behavioral tasks, we performed deep-brain Ca^{2+} imaging in freely moving mice through the use of a miniature microscope (Ghosh et al., 2011). We conducted three sequential behavioral tests, which included social preference, exposure to different tones, and classical fear conditioning (Figure 2A), in VIP-ires-cre mice microinjected with a Cre-dependent adeno-associated viral vector in the aIC to express the Ca^{2+} indicator GCaMP6s and implanted with a gradient refractive index (GRIN) lens above the injection site (Figures 2B, 2C, and S3A). To have the minimum carry-on effect of one test onto the other, the most stressful paradigm (fear conditioning) was the last to be performed (Figure 2A). Despite the temporal sequence of the behavioral tests, we first analyzed the recording of the activity of VIP+ INs in the aIC during the cued fear-conditioning paradigm, as this class of INs was previously shown to be recruited during the presentation of aversive stimuli in the BLA as well as in prefrontal cortex (Krabbe et al., 2019; Pi et al., 2013). In this test, an auditory conditioned stimulus (CS) is repeatedly paired with a mild aversive footshock (US) to elicit a fear response (Figures 2A and S3B). We found that US presentations induced higher general Ca^{2+} activity in the imaged neurons and recruited a larger population of active VIP+ INs compared with the CS presentations (67.1% active during US; 21.6% active during CS; chi-square, $p = 0.0001$; Figures 2D–2G and S4A). Upon retrieval of the fear memory a day later, in which the CS was not paired with the reinforcing US (CS-R), the average activity and fraction of active VIP+ INs during the CS presentation (30.4%; chi-square, $p = 0.42$) and during the US omission (US–) (22.8%; chi-square, $p = 0.45$) were comparable with those observed during the CS presentation in the fear acquisition phase (Figures S4A–S4E).

We then analyzed the response of aIC VIP+ INs to the pseudo-random presentation of two intermingled neutral auditory stimuli of identical frequency (6 kHz), but different intensity (50 versus 80 dB) (Figure 3A). We observed that VIP+ INs showed a higher activity and responded in a larger proportion to the 80 dB tone (38.2% during 80 dB and 21.1% during 50 dB presentations; chi-square, $p = 0.018$; Figures 3B–3D and S4A).

Finally, we examined aIC VIP+ IN responses during a modified version of the three-chamber social preference test (Nadler et al., 2004). For this test, each experimental mouse was subjected to the paradigm twice, with an inter-trial interval of 24 h and with the position of the object and novel interactor mouse exchanged (Figure 3E). As expected, mice spent more time interacting with the unfamiliar mouse compared with the object (Figure 3F). On day 1, the overall Ca^{2+} activity of VIP+ INs was significantly higher during epochs of social compared with object visits

(E) Sequential sections from an example mouse brain depicting representative monosynaptic inputs to aIC VIP+ INs. On the top, illustrations from the Allen Mouse Brain Atlas corresponding to the actual sections on the bottom. Areas with a particularly high content of first-order presynaptic neurons are indicated with different shades of gray, darker areas indicate higher density. Scale bar, 1 mm.

(F) Heatmap (left) and bar plot (right) representing fraction of inputs (%) over total input numbers for each identified brain area, with >1% of total input, projecting to aIC VIP+ INs. Data are shown as mean ± SEM.

(G) Representative image of retrogradely labeled neurons presynaptic to aIC VIP+ INs in the MD. Scale bar, 500 μm.

(H) Representative image of retrogradely labeled neurons presynaptic to aIC VIP+ INs in the SS and IC. Scale bar, 500 μm.

(I) Representative image of ChR2-mCherry immunolabeled axons in the mPFC and aIC originating from the MD. Scale bar, 1 mm.

(J) Representative high-magnification image of ChR2-mCherry-labeled axon terminals (green) and VIP immunoreactivity (magenta) in the aIC of a mouse injected with ChR2-mCherry in the MD.

Arrows indicate appositions of ChR2-mCherry-labeled boutons onto the soma and dendrites of VIP+ INs. Scale bar, 10 μm. Data are shown as mean + SEM. For anatomical abbreviations, see STAR Methods.

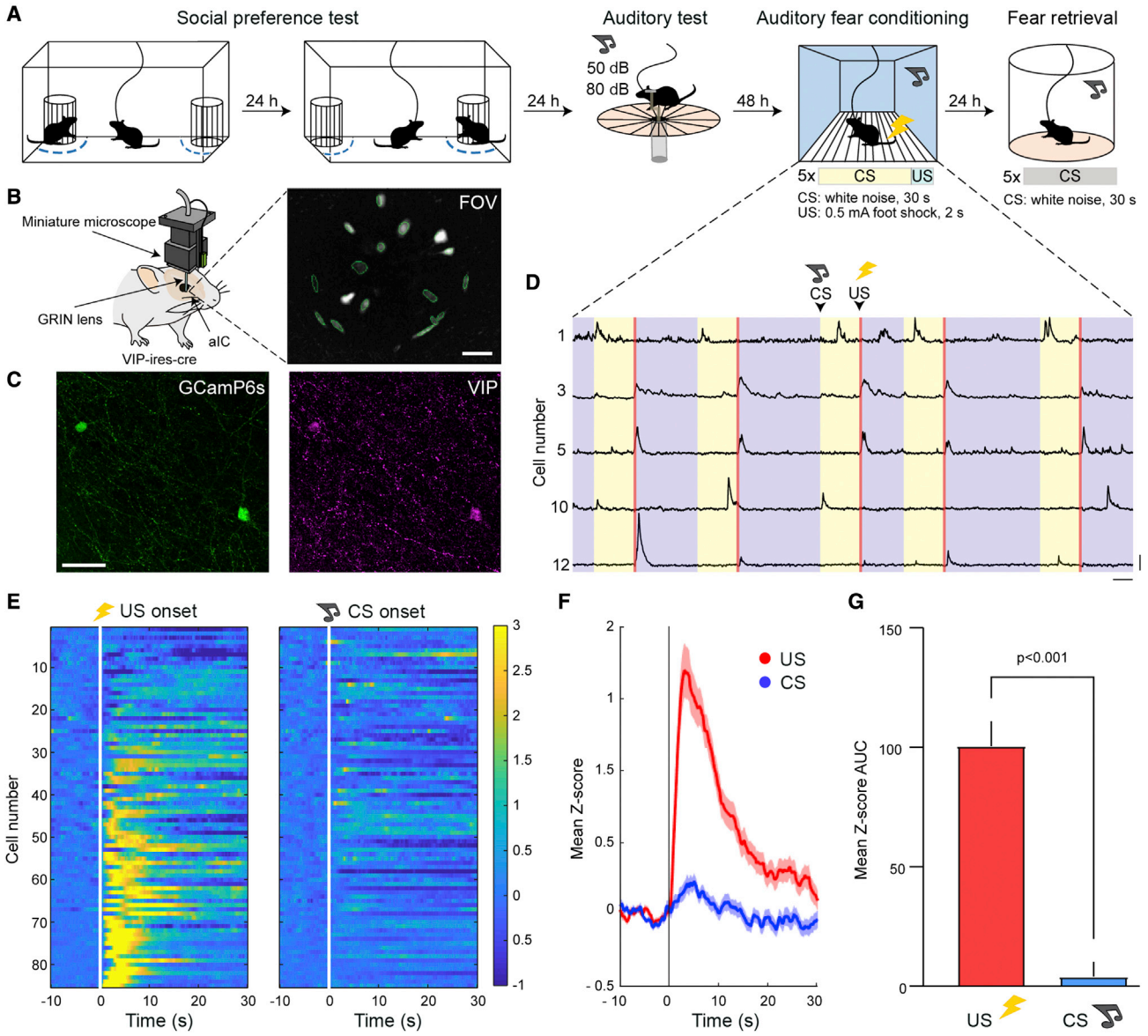

Figure 2. Aversive stimuli activate aIC VIP+ INs

(A) Diagram of the 5-day-long behavioral paradigm, including two consecutive social preference tests, auditory test, fear conditioning, and retrieval tests.

(B) Schematic of the experimental approach used for freely moving Ca^{2+} imaging of aIC VIP+ INs. Example of field-of-view (FOV) through the implanted GRIN lens with representative overlaid cell contours (in green). Scale bar, 100 μm.

(C) Representative confocal images showing the Cre-dependent GCaMP6 expression in VIP+ aIC INs (left panel) and VIP immunostaining (right panel). Scale bar, 20 μm.

(D) Ca^{2+} traces during the fear-conditioning session recorded from five VIP+ INs. Arrowheads indicate the onset of CS and US stimuli. Colors indicate stimulus presentation: yellow, CS; red, US; purple, ITI. Scale bars, horizontal 15 s, vertical 5 *Z* score.

(E) Activity heatmap from all individual recorded aIC VIP+ INs (n = 85 cells from N = 7 mice), sorted by time of peak activity during US presentations, averaged across all five trials, during US (left panel) and CS presentations (right panel). Heatmap scale bar represents *Z* score values.

(F) US and CS responses averaged from all recorded cells across all five trials.

(G) Mean area under the curve (AUC) of *Z* scored activity responses was significantly higher during US presentations compared with CS presentations (Wilcoxon signed rank, p = 0.0001, n = 85 cells).

Data are shown as mean + or ± SEM. Details of statistical analyses are provided in Table S1.

(Figures 3G–3I), although the response dynamic showed a slow increase that reached the maximal steady-state activity 3–4 s after the test animal was in close proximity to the wire cage containing the novel conspecific. Moreover, a larger proportion of aIC VIP+ INs were active during the interaction with the unfamiliar mouse in comparison with the object (42% and 13.6%,

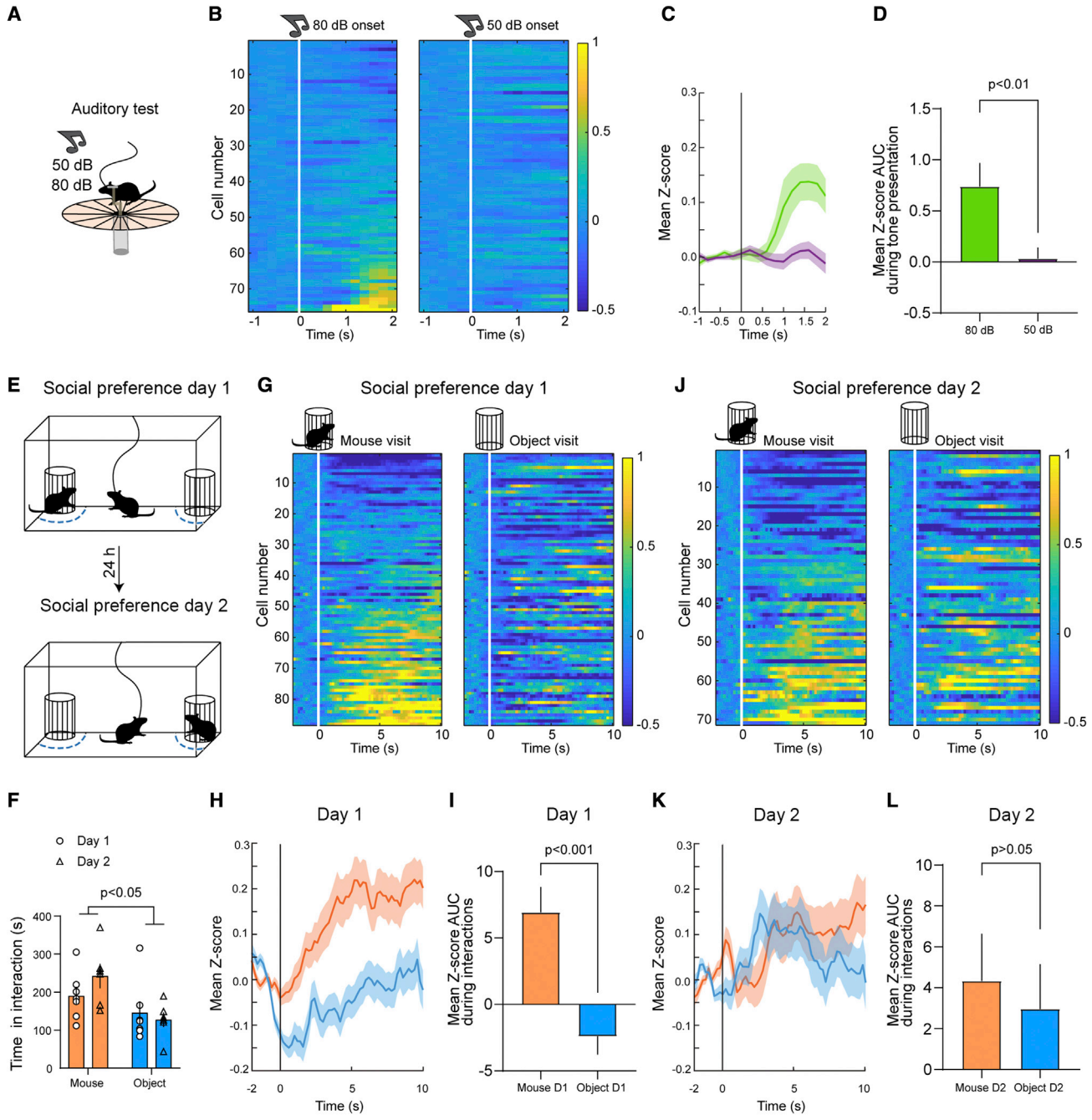

Figure 3. Auditory and social stimuli activate aIC VIP+ INs

(A) Schematic of the auditory response test, in which 30 tone presentations of 50 or 80 dB (6,000 Hz, for 1 s) were pseudo-randomly presented.

(B) Activity maps from all individual recorded aIC VIP+ INs (n = 76 cells from N = 7 mice), sorted by time of peak activity during the 80 dB tone presentations, averaged across all 80 dB (left panel) or 50 dB tone presentations (right panel).

(C) Eighty and 50 dB tone responses averaged from all recorded aIC VIP+ INs across all tone presentations.

(D) Mean AUC of *Z* scored activity responses was higher on 80 dB compared with 50 dB tone presentations (Wilcoxon signed rank, p = 0.003, n = 76 cells).

(E) Schematic of the social preference test on days 1 and 2 of testing. The position of the interactor mouse was counterbalanced between days.

(F) Time spent in interaction with the novel conspecific mouse or object during the two days of testing (mixed-effects model REML; main effect zone: p = 0.025; main effect day: p = 0.55; interaction effect: p = 0.26).

(G) Activity maps from all individual recorded aIC VIP+ INs on social preference test day 1 (n = 88 cells from N = 7 mice), sorted by time of peak activity during interactions with another conspecific mouse, averaged across all interactions with the conspecific (left panel) or object (right panel).

(H) Mouse and object interaction responses averaged from all recorded aIC VIP+ INs across all interactions.

(legend continued on next page)

respectively, chi-square, p = 0.0001; Figure S4A). On day 2, the number of active VIP+ INs responding to the new conspecific remained proportionally similar (38%) to day 1, likewise the global Ca^{2+} activity increased following the entry in the close proximity area and displayed a comparable response dynamic to the first trial. On the other hand, the number of VIP+ INs active during visits to the novel object doubled (30%; Figure S4A) when the mice were re-tested on the second day, and the Ca^{2+} activity showed a transient increase of a similar magnitude to the one observed during social visits (Figures 3J–3L). This unexpected increase in activity and number of VIP+ INs responding to the object on day 2 may result from a response to the omission of the social cue given that the novel conspecific and the object were switched on day 2. This would be consistent with what we observed during fear retrieval, where a substantial proportion of VIP+ INs responded to the omission of the US (Figure S4A).

Altogether, these results reveal that, at the population level, aIC VIP+ INs respond to aversive, social, and auditory stimuli during different behavioral constructs.

aIC VIP+ IN activity is required for aversive learning and social preference

If the activity evoked in aIC VIP+ INs by the US or interaction with a novel conspecific contributes to outcome prediction, then the suppression of these responses should decrease the efficacy of the CS-US association and intensity of social preference. To test this, VIP-ires-cre mice were bilaterally injected in the aIC with either a control viral vector expressing green fluorescent protein (GFP) or one expressing the inhibitory opsin archaerhodopsin (ArchT-GFP), and implanted with optic fibers above the injection sites (Figures 4A–4C and S5A). In a 10 min social preference test, we selectively triggered optogenetic silencing of aIC VIP+ INs only when mice were in close proximity to the unfamiliar interactor mouse during the last 5 min of the test (Figure 4D). ArchT- and GFP-injected animals did not differ in the time spent in the interaction zone of the conspecific (two-way ANOVA, interaction: p = 0.27; group: p = 0.18) and showed the known natural decline of social interaction with time (Figure 4E; time: p = 0.001). Similarly, the social interaction ratio for both GFP- and ArchT-injected groups was lower in the second 5 min of the test (two-way ANOVA, interaction: p = 0.15; time: p = 0.001; group: p = 0.45), although after post-hoc comparisons this effect resulted significant only for ArchT-injected mice (Figure 4F; Bonferroni multiple comparison test, p < 0.001). This prompted us to explore optogenetic inhibition of aIC VIP+ INs during the first 5 min, hence circumventing the confounding of the decline in social interaction with time. Indeed, when light was allowed to be delivered only during the first 5 min of the test (Figure 4G), ArchT-injected mice did not display a reduction in social preference in the last 5 min, whereas, as expected, GFP-injected animals were not affected in their natural behavior (Figure 4H). The social interaction ratio showed a significant group × time interaction (two-way ANOVA, interaction: p = 0.006), revealing that ArchT-injected mice interacted more with the novel conspecific, in comparison with the object, during the second half of the test (post-hoc Bonferroni multiple comparison test, p = 0.01) (Figure 4I). We further confirmed that the reduction in social preference did not result from a general aversive effect of optogenetic inhibition of aIC VIP+ INs by testing the animals in a real-time object place preference test (Figures S5B–S5D), or from an influence on locomotion (Figures S5E–S5G).

We next investigated whether the specific suppression of aIC VIP+ IN activity during the presentation of the footshock in cued fear conditioning influences associative learning (Figure 4J). GFP- and ArchT-injected mice displayed similar levels of freezing during the successive CS-US pairings in the acquisition phase (Figure 4K). However, when the animals underwent fear retrieval, 24 h later and in a different context, ArchT-injected mice froze significantly less compared with GFP-injected controls, but the percent of freezing remained significantly higher compared with the pre-CS (two-way ANOVA, group: p = 0.001; time: p = 0.001; interaction: p = 0.03; Bonferroni multiple comparisons test, Pre-CS-R GFP versus Pre-CS-R ArchT: p = 0.99; CS-R GFP versus CS-R ArchT: p = 0.001), indicating that the light-mediated inhibition of aIC VIP+ INs during the CS-US pairings did not prevent the formation of the fear memory (Figure 4L).

Taken together, these data suggest that the activity of aIC VIP+ INs during the exposure to social or aversive stimuli is necessary for the full expression of both social preference and fear memory retrieval.

Based on our optogenetic interrogations, we hypothesized that the general activity of aIC VIP+ INs decays with time or with the repetitive presentation of a given stimulus during social interactions and fear learning. Indeed, during the social preference test, the general activity of aIC VIP+ INs was higher during the exploration of an unfamiliar mouse compared with the object only in the first 5 min of the test, and also compared with the last 5 min of social interaction. On the other hand, the activity related to the novel object increased between the first and last 5 min on day 1 (Figures 5A and 5B). Upon replication of the same behavioral paradigm 24 h later, the temporal difference in activity between social and non-social exploration remained stable (Figure 5C). Similarly, while CS presentations elicited a similar activity in aIC VIP+ IN throughout fear acquisition, the activity of these INs decreased with successive US presentations (Figures 5D and 5E). During fear retrieval, the initial CS presentation induced a higher response compared with the one elicited during fear conditioning (Mann-Whitney, CS1 versus CS-R1,

(I) Mean AUC of *Z* scored activity responses was significantly higher during interactions with a mouse compared with object interactions on day 1 (Wilcoxon signed rank, p = 0.0002, n = 88 cells).

(J) Activity maps from all individual recorded aIC VIP+ INs on social preference test day 2 (n = 71 cells from N = 6 mice), sorted by time of peak activity during interactions with another conspecific mouse, averaged across all interactions with the conspecific (left panel) or object (right panel).

(K) Mouse and object interaction responses averaged from all recorded aIC VIP+ INs across all interactions.

(L) Mean AUC of *Z* scored activity responses was similar during interactions with the mouse or object on day 2 (Wilcoxon signed rank, p = 0.31, n = 71 cells).

Data are shown as mean + or ± SEM. Details of statistical analyses are provided in Table S1.

CellPress
OPEN ACCESS

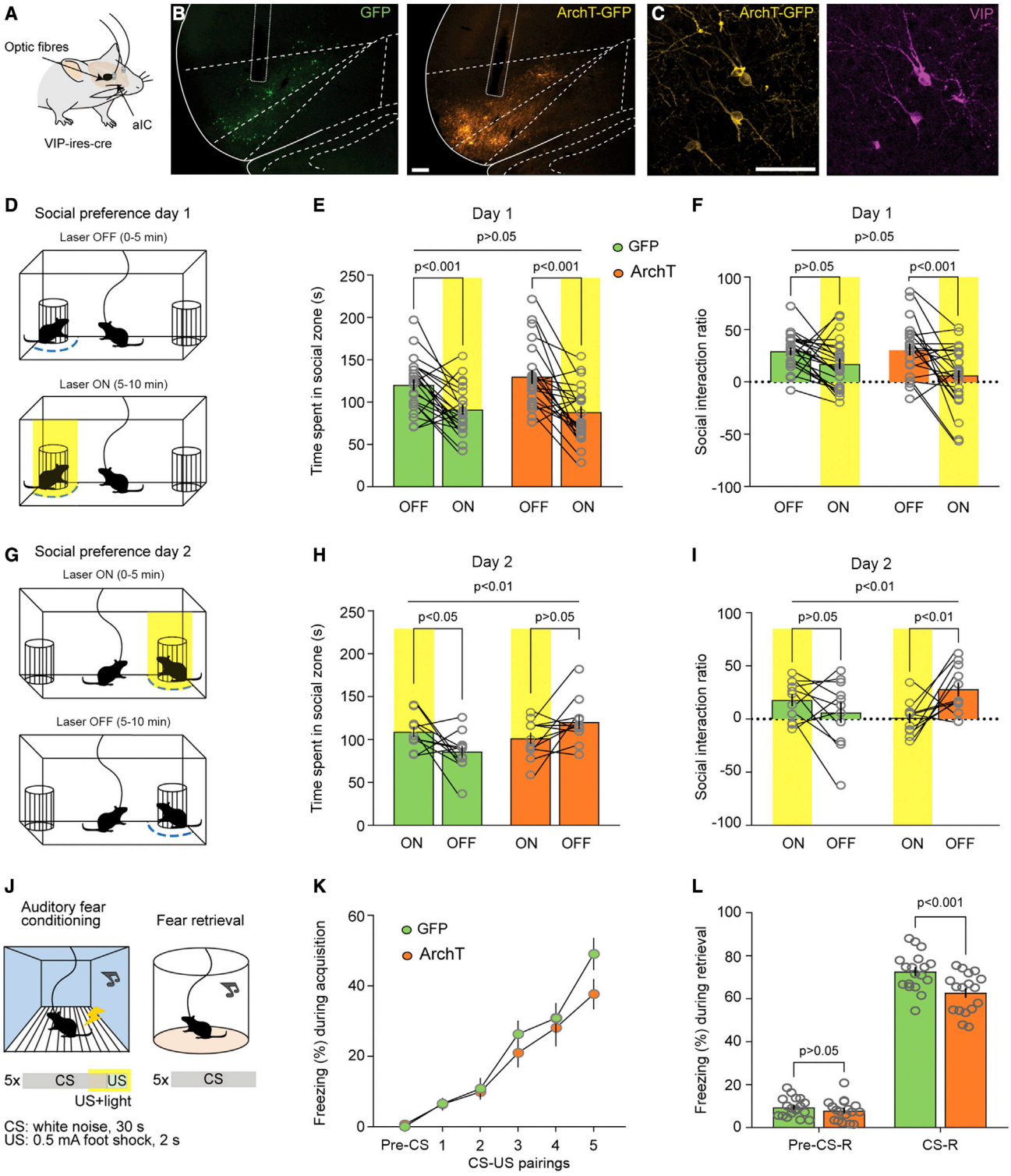

Figure 4. aIC VIP+ IN activity is required for aversive learning and social preference

(A) Schematic of the approach used for optogenetic loss-of-function experiments.

(B) Example micrographs of injection and implantation sites of GFP-only (left) or ArchT-GFP (right) in the aIC of VIP-ires-cre mice. Scale bar, 200 μm.

(C) Example of ArchT selective expression in aIC VIP+ INs. Scale bar, 20 μm.

(D) Social preference paradigm for closed-loop light-induced suppression of aIC VIP+ IN activity during close interactions with a novel conspecific on day 1 of testing, during the second 5 min of the test.

(legend continued on next page)

p = 0.025), which progressively diminished with consecutive presentations of the CS, whereas the unexpected omission of the US led to a delayed increase in activity (Figure 5F).

aIC VIP+ INs are functionally heterogeneous

Our analyses of deep-brain Ca^{2+} imaging showed that footshocks during fear conditioning and close interactions with a novel conspecific strongly triggered the activity of a large fraction of aIC VIP+ INs. We next sought to assess the coding specificity of these INs for specific behavioral epochs. In other words, whether different functional populations among aIC VIP+ INs exist that selectively respond to distinct stimuli.

During the first social preference test day, the number of active coding neurons (CNs) for the interaction with the unfamiliar mouse (classified as having a mean activity Z score 2σ above baseline, but not during object interactions; see STAR Methods) was larger than those specifically coding for the object (chi-square, p = 0.0004; Figures 6A and 6B). On the second day, a similar proportion of CNs responded to the novel mouse and the object (chi-square, p = 0.14; Figures 6E and 6F). However, activity patterns of CNs during the social interaction test did not change across days: mouse CNs were highly active during interactions with a conspecific mouse but not with the object, whereas object CNs were active during interactions with the empty wire cage and not with the novel mouse (Figures 6C, 6D, 6G, and 6H).

During the fear-conditioning acquisition phase (Figure 6I) the number of CNs activated upon US presentations was higher than those exclusively activated by CS presentations (chi-square, p = 0.0001), whereas the opposite was observed for inhibited neurons (Figure 6J). The activity patterns during US presentations showed that US CN activity reached its maximum a few seconds after the shock and persisted for the entire period analyzed (30 s), whereas CS CNs, after an initial peak of activity, became strongly inhibited (Figures 6K and 6L). During CS presentations, US CNs remained unresponsive, whereas CS CNs steadily increased their activity (Figures 6K and 6L). During the fear retrieval phase (Figure 6M), a higher proportion of neurons coded for CS presentations (CS-R CNs) compared with the fear acquisition phase (Figure 6N; chi-square, p = 0.009). However, the amount of VIP+ INs that responded to the omission of the US (US- CNs) was comparable with the fraction of CS-R CNs (Figures 6M and 6N; chi-square, p = 0.43). The activity patterns of these two functional ensembles, namely CS-R and US- CNs, showed a strong negative correlation (Figures S6A, S6B, S6D, and S6E). During CS presentations, CS-R CNs were highly active, while US- CNs were strongly inhibited. Conversely, during US omissions US- CNs were highly active, while CS-R CNs were strongly inhibited (Figures 6O and 6P). Altogether, these results suggest that, despite the fact that the presentation of social and aversive stimuli leads to an overall increase in the activity of aIC VIP+ INs, a broad functional heterogeneity exists in the individual responses of these cells.

We next addressed whether a loss in coding fidelity of CNs underlies the decay in the general activity of VIP+ INs upon repeated stimulus presentations. To this aim, we calculated the Mahalanobis population vector distance (PVD) to assess the differentiability of the responses (Grewe et al., 2017). During the social preference behavioral paradigm, the minimum duration of the interaction with a given stimulus across all imaged mice (i.e., maximum object interaction during day 1 or 2 of the social interaction test) was used as the maximum period considered for analysis of PVD. We found that, only during the first day of testing, object and mouse CN PVDs significantly increased over time, owing to increased fidelity of the VIP+ IN coding ensembles to the social or object cues (Figures 6Q and 6R). In the course of fear conditioning and retrieval, although the activity of CS, US, CS-R, or US- CNs changed across successive trials (Figures S6C and S6F), PVDs between CN ensembles remained unchanged (Figures 6S and 6T). These data show that the observed decrease in general activity upon repeated stimulus presentation does not arise from a loss or switch in

(E) The time spent in the social interaction zone was similar between ArchT- and GFP-injected animals during periods of OFF (first 5 min) and ON (last 5 min) laser-mediated inhibition (two-way ANOVA, main effect group: p = 0.67; main effect time: p = 0.001; interaction effect: p = 0.27; Bonferroni multiple comparisons test, OFF GFP versus ON GFP, p = 0.001; OFF ArchT versus ON ArchT, p = 0.001).

(F) Social interaction ratios during periods of OFF (first 5 min) and ON (last 5 min) laser-mediated inhibition in ArchT- and GFP-injected animals (two-way ANOVA, main effect group: p = 0.45; main effect time: p = 0.001; interaction effect: p = 0.15; Bonferroni multiple comparisons test, OFF GFP versus ON GFP, p = 0.15; OFF ArchT versus ON ArchT, p = 0.001).

(G) Social preference paradigm for specific suppression of aIC VIP+ IN activity during interactions with a novel conspecific on day 2 of testing, during the first 5 min of the test.

(H) Time spent in the social interaction zone differed between ArchT- and GFP-injected animals. While GFP-injected mice showed decreased social interaction time during the last 5 min of the test, ArchT-injected animals did not (two-way ANOVA, main effect group: p = 0.08; main effect time: p = 0.75; interaction effect: p = 0.004; Bonferroni multiple comparisons test, OFF GFP versus ON GFP, p = 0.04; OFF ArchT versus ON ArchT, p = 0.11).

(I) Social interaction ratios in ArchT-injected animals during periods of ON (first 5 min) laser-mediated inhibition were lower than in OFF periods compared with GFP-injected animals (two-way ANOVA, main effect group: p = 0.74; main effect time: p = 0.23; interaction effect: p = 0.006; Bonferroni multiple comparisons test, OFF GFP versus ON GFP, p = 0.42; OFF ArchT versus ON ArchT, p = 0.01).

(J) Fear conditioning paradigm for closed-loop suppression of aIC VIP+ IN activity during CS-US pairings (left panel). Fear retrieval was performed in a different context presenting five times the same CS (right panel).

(K) Optogenetic inhibition of VIP+ aIC IN activity during fear conditioning does not affect associative learning as measured by freezing responses to CS 1–5 (two-way ANOVA, main effect group: p = 0.33; main effect time: p = 0.0001; interaction effect: p = 0.2117).

(L) Optogenetic inhibition of aIC VIP+ IN activity during fear conditioning reduces the strength of associative learning as measured by freezing responses to CS-R 1–5 on retrieval testing (two-way ANOVA, main effect group: p = 0.001; main effect time: p = 0.001; interaction effect: p = 0.03; Bonferroni multiple comparisons test, Pre-CS-R GFP versus Pre-CS-R ArchT, p = 0.99; CS-R GFP versus CS-R ArchT, p = 0.001).

Data are shown as mean ± SEM. Details of statistical analyses are provided in Table S1.

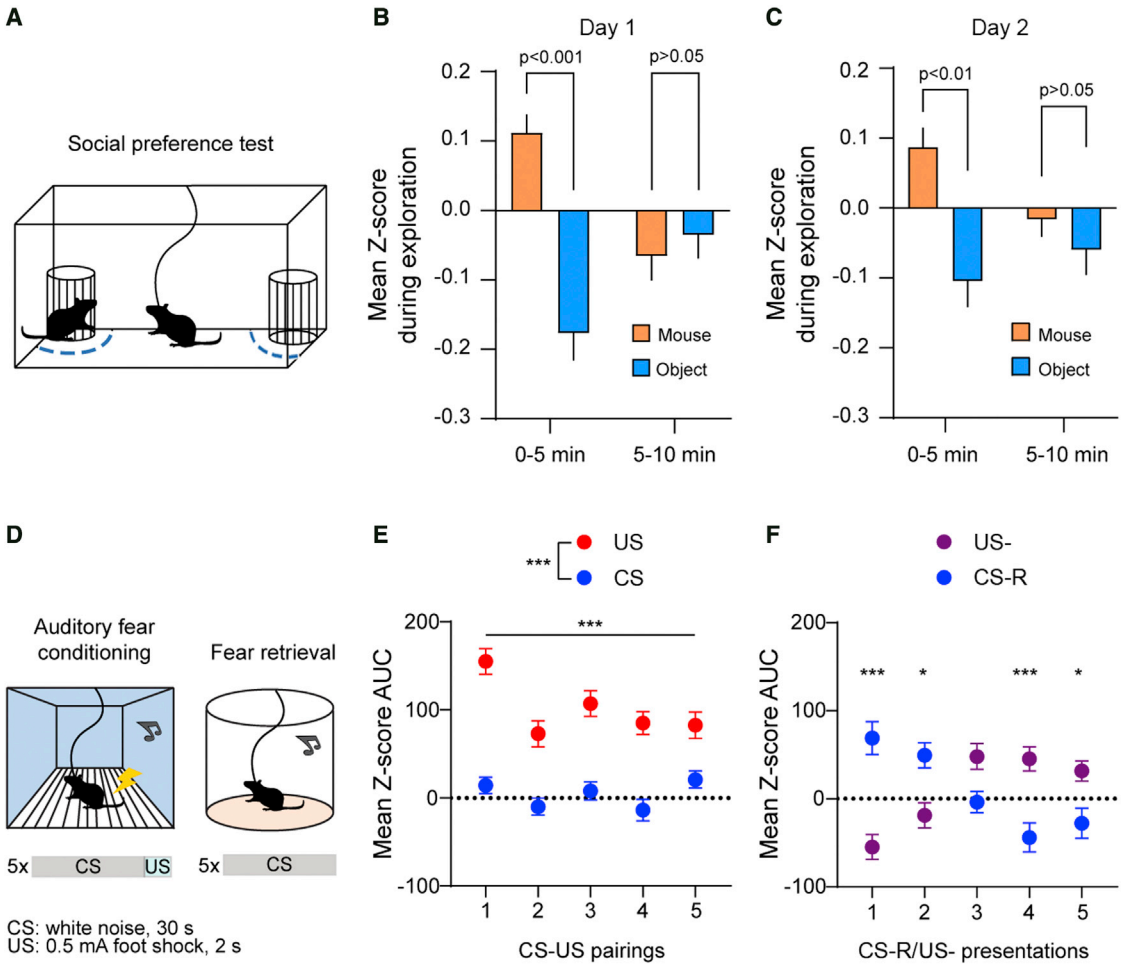

Figure 5. aIC VIP+ INs activity decays with repeated stimuli presentations

(A) Diagram of the social preference test.

(B) The mean *Z* scored activity of aIC VIP+ INs during the exploration of an unfamiliar conspecific was significantly higher compared with the activity during the exploration of a novel object on day 1, but only during the first 5 min of the test (two-way ANOVA, main effect interaction zone: p = 0.005; main effect time: p = 0.48; interaction effect: p = 0.0001; Bonferroni multiple comparisons test, mouse versus object 0–5 min, p = 0.0001; mouse versus object 5–10 min, p = 0.98; mouse 0–5 min versus 5–10 min, p = 0.0003; object 0–5 min versus 5–10 min, p = 0.0037).

(C) Similar to day 1, the mean *Z* scored activity of aIC VIP+ INs on day 2 during the exploration of an unfamiliar conspecific was higher than during the exploration of a novel object only in the first 5 min of the test (two-way ANOVA, main effect interaction zone: p = 0.004; main effect time: p = 0.24; interaction effect: p = 0.04; Bonferroni multiple comparisons test, mouse versus object 0–5 min, p = 0.0006; mouse versus object 5–10, min p = 0.76; mouse 0–5 min versus 5–10 min, p = 0.08; object 0–5 min versus 5–10 min, p = 0.75).

(D) Diagram of the fear conditioning (left panel) and retrieval (right panel) paradigms.

(E) Mean *Z* score AUC elicited by individual CS or US presentations during fear conditioning (two-way ANOVA, main effect pairing: p = 0.0001; main effect stimulus: p = 0.0001; interaction effect: p = 0.009; Bonferroni multiple comparisons test, US1 versus US2, p = 0.0001; US1 versus US3, p = 0.02; US1 versus US4, p = 0.0001; US1 versus US5, p = 0.0001).

(F) Mean *Z* score AUC elicited by individual CS-R or the omission of the US (US-) during fear retrieval (two-way ANOVA, main effect pairing: p = 0.11; main effect stimulus: p = 0.92; interaction effect p = 0.0001; Bonferroni multiple comparisons test, US-1 versus CS-R1, p = 0.0001; US-2 versus CS-R2, p = 0.01; US-3 versus CS-R3, p = 0.09; US-4 versus CS-R4, p = 0.0003; US-5 versus CS-R5, p = 0.03).

Data are shown as mean + or ± SEM. *p < 0.05, **p < 0.01, ***p < 0.001. Details of statistical analyses are provided in Table S1.

the coding specificity of the different functional populations of aIC VIP+ INs, but rather results from a mechanism of repetition suppression (Henson and Rugg, 2003; Zweynert et al., 2011).

We further examined whether individual aIC VIP+ INs maintained their coding specificity across days. To this aim, we registered their activity in the two consecutive days of social preference testing (Figure 7A). We found that only a minority of mouse CNs (n = 3/14, 21.4%) and object CNs (n = 1/4, 25%) maintained their coding specificity across days (Figure S7). A similar number of day 1 mouse CNs responded non-specifically to both object and mouse interactions on the second day (n = 4/14, 28.5%), or stopped responding (n = 6/14, 42.9%).

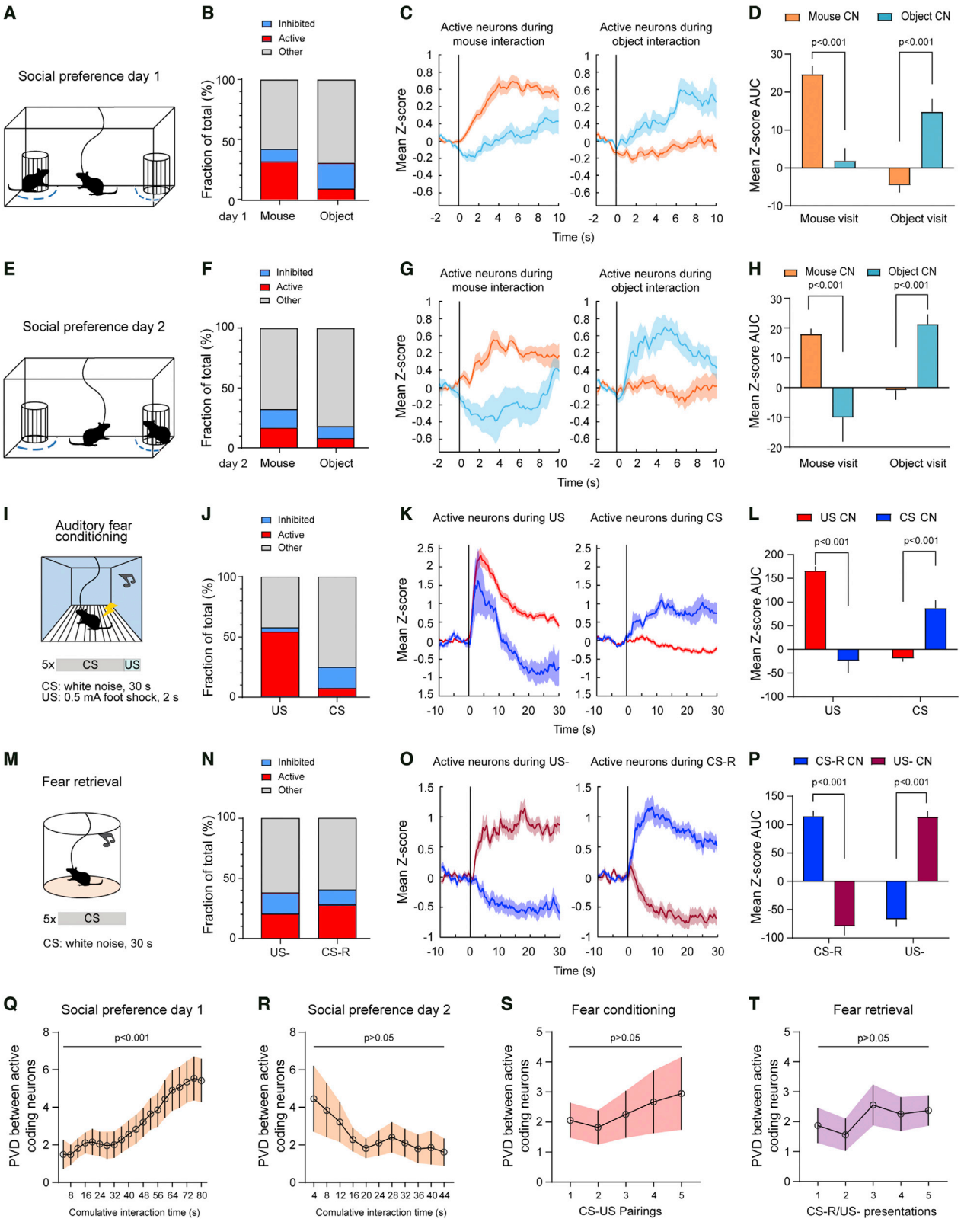

(legend on next page)

These data reveal complex and dynamic changes of VIP+ IN responses during exploration of social and non-social cues.

Finally, to determine whether individual aIC VIP+ INs respond specifically to either stimuli of social or aversive nature, we registered the activity of these INs across the different behavioral paradigms (Figure 7A). A large proportion of mouse CNs on both days 1 and 2 were found to respond to the US (day 1: n = 12/13, 92.3%; day 2: n = 5/7, 71.4%; Figure 7B) during fear conditioning, whereas only a minority were responsive to the CS (day 1: n = 1/13, 7.7%; day 2: n = 1/7, 14.2%; Figure 7B). During fear retrieval, most of the mouse CNs either responded to the CS-R or stopped responding, whereas only a few were activated during the US omission (day 1: CS-R n = 6/15, 40%, US- n = 1/15, 6.6%; day 2: CS-R n = 4/9, 44.4%, US- n = 1/9, 11.1%; Figure 7C).

Taken together, our data show that individual VIP+ INs within the aIC respond to both aversive and social stimuli irrespective of sensory modality and potentially value.

DISCUSSION

Here, we show that aIC VIP+ INs respond, both at the population and individual neuron level, to different sensory stimuli independent of task and modality using single-cell Ca^{2+} imaging, and that these INs are anatomically connected to a wide range of sensory-related brain areas. Optogenetic inhibition of aIC VIP+ INs during the exposure of the animals to social or aversive stimuli impaired the full expression of both social preference and fear memory retrieval. Moreover, after deriving the coding specificity of these INs, we observed that functional responses to different stimuli, such as social versus non-social cues, are encoded by specialized subsets of VIP+ INs, although their coding stability and specificity is flexible across days and behavioral paradigms. Therefore, our findings suggest that the activity of aIC VIP+ INs is required for the processing of behaviorally relevant sensory stimuli within the aIC, which in turn modulates the efficacy of associative learning (Hersman et al., 2020; Holland, 1980).

Our tracing experiments identified direct inputs to aIC VIP+ INs from major sensory processing-related areas, such as the thalamus, orbitofrontal cortical areas, amygdala and basal forebrain. Of note is the preferential connectivity of MD neurons to aIC VIP+ INs among thalamic nuclei. This finding supports a participation of these INs in sensory processing to enable behavioral adaptations, since the MD is considered the main SN hub within the thalamus (Menon, 2015) and has been shown to modulate salience of fear-associated cues (Zhou et al., 2021; Lee et al., 2012) as well as social-related behaviors (Zhou et al., 2017; Ferguson and Gao, 2018). Interestingly, MD afferents were also shown to target VIP+ INs in the mPFC (Anastasiades et al., 2021), which raises the possibility for the existence of a conserved bottom-up functional modulation of sensory processing through MD connectivity onto VIP+ INs in these neocortical regions.

Gehrlach et al. (2020) recently found a connectivity pattern of aIC GABAergic neurons consistent with our findings for VIP+ INs, although with a few dissimilarities. In particular, we observed a

Figure 6. aIC VIP+ INs are a heterogeneous functional population

(A and E) Schematic of the social preference paradigm on days 1 and 2 of testing.

(B and F) Percentage of active or inhibited aIC VIP+ CN during distinct stimulus presentations on days 1 and 2 of social preference testing. Non-coding neurons are referred as other.

(C and G) Averaged responses from recorded aIC VIP+ mouse CN (orange) or object CN (turquoise) across all mouse and object interactions on day 1 (C) and day 2 (G).

(D and H) Mean AUC of *Z* scored activity responses during interactions with the conspecific was higher for mouse CN than for object CN, while the latter were preferentially active during interactions with the novel object on day 1 (two-way ANOVA, main effect ensemble: $p = 0.602$; main effect visit: $p = 0.0068$; interaction effect: $p = 0.0001$; Bonferroni multiple comparisons test, mouse CN versus object CN: object visit, $p = 0.0001$, mouse visit, $p = 0.0001$; object visit versus mouse visit: mouse CN, $p = 0.0001$, object CN, $p = 0.02$) and day 2 (two-way ANOVA, main effect ensemble: $p = 0.43$; main effect visit: $p = 0.15$; interaction effect: $p = 0.0001$; Bonferroni multiple comparisons test, mouse CN versus object CN: object visit, $p = 0.0007$, mouse visit, $p = 0.0001$; object visit versus mouse visit: mouse CN, $p = 0.0024$, object CN, $p = 0.0006$).

(I) Schematic of the fear-conditioning paradigm.

(J) Percentage of inhibited or active aIC VIP+ CN during CS and US presentations (n = 85).

(K) Averaged responses from recorded aIC VIP+ US CN (red) and CS CN (blue) across all trials.

(L) Mean AUC of *Z* scored activity responses following US presentations was higher for US CN than for CS CN, while the latter were preferentially active during CS presentations (two-way ANOVA, main effect ensemble: $p = 0.0004$; main effect presentation: $p = 0.042$; interaction effect: $p = 0.0001$; Bonferroni multiple comparisons test, US CN versus CS CN: CS presentation, $p = 0.0001$, US presentation, $p = 0.0001$; CS versus US presentation: US+ CN, $p = 0.0001$, CS+ CN, $p = 0.0028$).

(M) Schematic of the fear retrieval paradigm.

(N) Percentage of aIC VIP+ INs with increased or decreased ($\pm 2\sigma$ over baseline) Ca^{2+} responses during CS-R or US- (n = 79).

(O) Averaged responses from recorded aIC VIP+ US- CN (magenta) and CS-R CN (blue) across all trials.

(P) Mean AUC of *Z* scored activity responses following CS-R presentations was higher for CS-R CN than for US- CN, while the latter were preferentially active during US omissions (main effect ensemble: $p = 0.407$; main effect presentation: $p = 0.719$; interaction effect: $p = 0.0001$; Bonferroni multiple comparisons test, US- CN versus CS-R CN: CS-R presentation, $p = 0.0001$, US- presentation, $p = 0.0001$; CS-R versus US- presentation: US- CN, $p = 0.0001$, CS-R CN, $p = 0.0001$).

(Q) Population vector distances between clusters of mouse and object CN at different cumulative times of interaction with the object or mouse on social preference test day 1 (Friedman test, $p < 0.0001$).

(R) Population vector distances between clusters of mouse and object CN at different cumulative times of interaction with the object or mouse on social preference test day 2 (Friedman test, $p = 0.13$).

(S) Population vector distances between clusters of CS and US CN at different CS-US pairings during fear conditioning (Friedman test, $p = 0.93$).

(T) Population vector distances between clusters of CS-R and US- CN at different CS-R/US- presentations during fear retrieval testing (Friedman test, $p = 0.13$).

Data are shown as mean + or ± SEM. Details of statistical analyses are provided in Table S1.

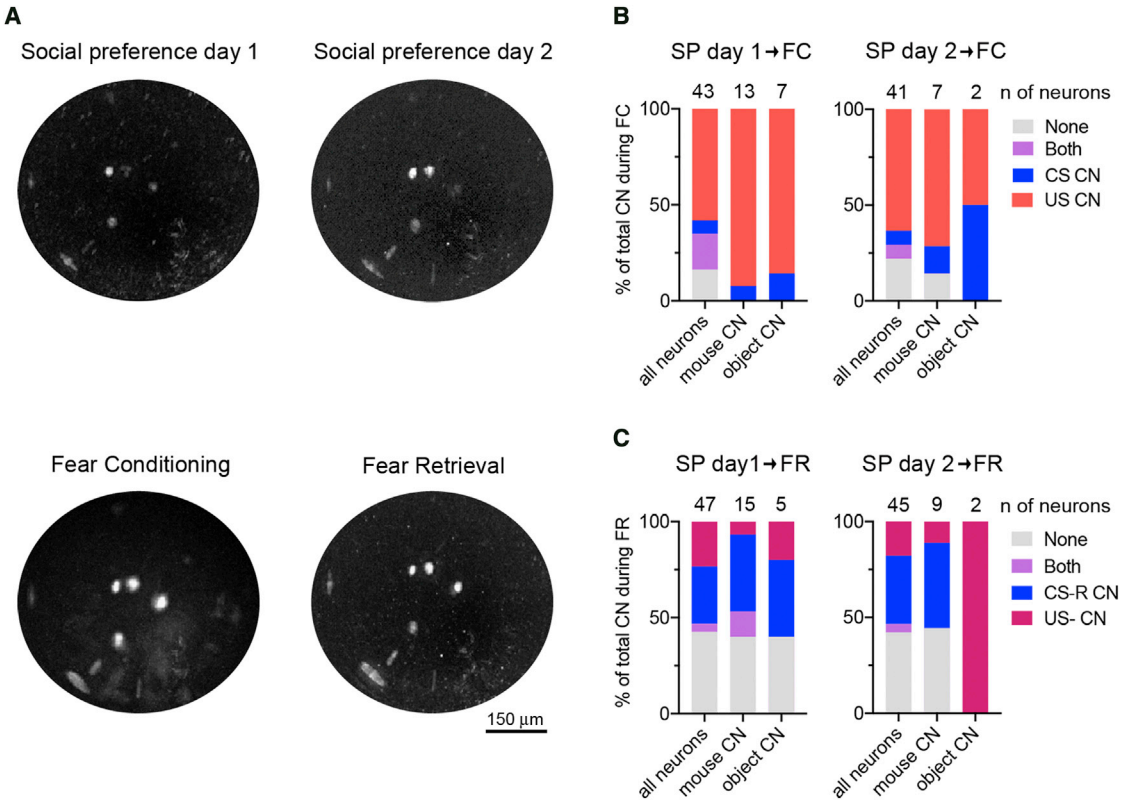

Figure 7. Parallel coding of aversive and social stimuli in aIC VIP+ INs

(A) Example images of GCamP6s-dependent signals in aIC VIP+ INs within the FOV during the social preference test on day 1 (top left) and day 2 (top right), during fear conditioning (bottom left) and fear retrieval (bottom right).

(B) Percentage of mouse and object CNs on day 1 (left) and day 2 (right) that were also responding to the US, CS, both, or were unresponsive during fear conditioning.

(C) Percentage of mouse and object CNs on day 1 (left) and day 2 (right) that were also responding to the US-, CS-R, both, or were unresponsive during fear retrieval.

negligible number of presynaptic neurons providing first-order input to VIP+ INs in the ventral complex of thalamic nuclei and olfactory areas compared with GABAergic INs taken as a whole. Moreover, the presynaptic neurons in the piriform cortex targeting VIP+ INs were proportionally much higher than those reported for aIC GABAergic INs. These dissimilarities support the view that different cortical INs are characterized by a distinct pattern and relative weight of long-range presynaptic inputs (Ma et al., 2021; Naskar et al., 2021). We cannot, however, exclude at present that methodological differences between our study and the one by Gehrlach et al. (2020), e.g., the retrograde tracing efficacy or tropism of the rabies virus used, might have contributed to these differences. Further studies will have to address this potential issue and could include inputs to other IN types to provide a better understanding of the connectivity patterns of inhibitory circuits of the aIC.

The IC is a complex structure that can be divided into an anterior and a posterior part. They markedly differ in their connectivity with other brain regions and subserve different functions (Gehrlach et al., 2020; Gogolla, 2017; Livneh and Andermann, 2021). At the interface between these two parts, a middle insular zone exhibits mixed anterior and posterior connectivity features (Uddin et al., 2017; Gehrlach et al., 2020). Our study focused on the aIC given its primary involvement in multisensory and multimodal responses (Beer et al., 2013; Uddin, 2015; Uddin et al., 2017) in the social (Miura et al., 2020) and negative valence domains (Wu et al., 2020). In line with the known dense connectivity between the aIC and pIC, we found a large number of presynaptic neurons in the pIC innervating aIC VIP+ INs. This suggests that information related to salient sensory stimuli is also transmitted from the pIC to aIC VIP+ INs. Our study shows that aIC VIP+ INs were strongly activated by footshocks during the acquisition of fear conditioning, although their inhibition during the US presentation did not affect fear expression. On the other hand, upon fear memory retrieval we found a reduced freezing behavior that we attribute to a decrease in stimulus salience and consequently in the strength of the associative learning. Interestingly, subsets of pIC principal neurons are known to respond also to acute sensory nociceptive stimuli (tail shocks) and their silencing impaired the emergence of sustained states of anxiety without altering acute responses (Gehrlach et al., 2019), consistent with our findings in aIC VIP+ INs.

Cortical VIP INs were shown to play an important role in shaping responses to sensory inputs. For example, the activity

of VIP+ INs enhances the gain of visual and auditory responses (Fu et al., 2014; Letzkus et al., 2011; Pi et al., 2013; Cone et al., 2019; Keller et al., 2020), and in the visual cortex it was driven by the presentation of novel images or stimuli with high contrast, whereas it was suppressed by familiar images (Garrett et al., 2020). These findings are consistent with our own data and suggest a broad involvement of these INs in gain modulation to facilitate the encoding of salient stimuli. Furthermore, VIP+ INs in the auditory and prefrontal cortex were shown to respond to reinforcement signals, including reward and punishment (Letzkus et al., 2011; Pi et al., 2013). Only a few studies, however, have causally linked the function of VIP+ INs to distinct behavioral responses (Lee et al., 2019; Krabbe et al., 2019). In these studies, functional inhibition of VIP+ INs during aversive state processing led to decreased expression of anxiety or fearful states. This led us to hypothesize that the activity of VIP+ INs has an impact on the strength of learning associations and behavioral outcomes. In our work using closed-loop optogenetic experiments, we could demonstrate that inhibition of aIC VIP+ INs resulted not only in reduced fear memory retrieval, but also in a reduced approach to social cues.

Therefore, we posit that these INs prime the appraisal by the aIC of environmental signals with emotional value and govern behavioral adaptations. An interesting open question is whether aIC VIP+ INs achieve this by increasing neural gain, thus optimizing signal discrimination to enhance encoding of behaviorally relevant information (Ferguson and Cardin, 2020).

An interesting aspect of the activity of cortical VIP+ INs in response to different stimuli is its gradual decrease upon successive presentations (Garrett et al., 2020; Krabbe et al., 2019), a phenomenon known as repetition suppression. Repetition suppression is a general mechanism by which the magnitude of event-related responses, e.g., to a given stimulus, diminishes with its repeated presentation (Ishai et al., 2004; Henson and Rugg, 2003). Similarly, our data show that, during fear conditioning, the activity of aIC VIP+ INs decreased after the initial US presentation. In addition, upon fear memory retrieval, the response of these INs to repetitive CS presentations also declined. Consistent with the classical notion that the interest in a novel conspecific mouse naturally decays with time (Bariselli et al., 2016; Nadler et al., 2004), our work demonstrates that inhibition of aIC VIP+ INs during the initial phase of the sociability test reduces social preference. Our imaging data further corroborate the link between the decay of social preference with time and a reduction in activity of these INs. Remarkably, during the omission of the US, aIC VIP+ INs did not follow repetition suppression mechanisms, but rather displayed a delayed increase of their activity. Our data are in line with the recent finding in the visual cortex that VIP+ INs showed ramping activity upon stimulus omission from an expected sequence (Garrett et al., 2020). Similarly, the increase in activity upon interaction with the object on day 2 of the social preference test might reflect the absence of the conspecific in its previous location. Future research could address whether this increase in activity upon stimulus omission reflects a change in the homeostatic behavioral state of the animal without the presence of a sensory stimulus or, alternatively, serves as a temporal attention signal (Garrett et al., 2020; Nobre and Van Ede, 2018).

In our study, we show that although aIC VIP+ INs, when taken as a whole, respond to a variety of sensory cues, diverse functional ensembles are recruited in response to discrete stimuli (e.g., social versus non-social cues). The coding specificity of these functional ensembles of VIP+ INs resulted unstable across testing days and paradigms and revealed that diverse stimuli do not engage distinct aIC VIP+ INs but rather recruit the same population of VIP+ INs within the aIC. Our data further reveal that repetition suppression of aIC VIP+ IN activity cannot be explained by opposing roles or coding disruption of these different functional ensembles during a given test. This functional heterogeneity, however, can be accounted for by several factors, such as different intrinsic anatomical and physiological properties of VIP+ IN subclasses in relation to sensory processing (Guet-Mccreight et al., 2020). Alternatively, different aIC VIP+ INs may receive inputs only from specific subsets of the presynaptic areas that were identified by our viral tracing experiments, and hence would be embedded into distinct brain networks. An open question remains as to whether, at an individual neuronal level, specialized subsets of VIP+ INs encode independent components of sensory stimuli, such as perceptual salience or unexpectedness.

Atypical aIC activity has been considered a hallmark of autism (Di Martino et al., 2009; Uddin and Menon, 2009; Uddin, 2015; Uddin et al., 2013; Odriozola et al., 2016), schizophrenia (Wylie and Tregellas, 2010), and anxiety disorders (Terasawa et al., 2013; Alvarez et al., 2015). Substantial evidence also indicates that these disorders are characterized by an impairment in sensory processing (Uddin et al., 2013; Kapur, 2003; Pannekoek et al., 2013). A recent study has shown that early postnatal disruption of VIP+ IN function leads to long-term dysregulation of cortical activity and sensory learning (Batista-Brito et al., 2017). In a mouse model of Dravet syndrome, a severe neurodevelopmental disorder characterized by autism and epilepsy, VIP+ INs showed lasting firing abnormalities, unlike other cortical INs (Goff and Goldberg, 2019). Furthermore, loss of function of the autism-related protein Mecp2 in VIP+ INs was found to induce social preference deficits (Mossner et al., 2020). Therefore, failures in the encoding of sensory stimuli and behavioral relevance attribution by impaired VIP+ IN function could lead to atypical insula activity during stimulus processing, contributing to anxiety and/or autism spectrum disorder core symptoms.

In conclusion, our study identifies VIP+ INs, a subclass of INs that barely accounts for 2% of neocortical neurons (Connor and Peters, 1984), in the aIC as critical mediators for the encoding of information about behaviorally relevant environmental stimuli.

Limitations of the study

VIP+ INs in the barrel cortex show significant morphological and physiological differences according to their location in different layers (Prönneke et al., 2015). Our *in vivo* deep-brain Ca^{2+} imaging and optogenetic manipulations did not allow to address neurons in specific cortical layers due to several technical limitations (e.g., size and implantation of the GRIN lens or optical fiber). Therefore, we cannot exclude to have preferentially imaged or manipulated specialized subsets of aIC VIP+ INs. Future studies, will have to explore the existence of layer-specific and

functionally specialized subpopulations of these INs in sensory processing.

Despite the fact that optogenetic manipulations are commonly used to infer the contribution of discrete cell classes in specific behaviors, they can also result in complex and sometime paradoxical effects by shifting the excitation/inhibition balance of neural circuits (Ferguson and Cardin, 2020). Our optogenetic inhibition of aIC VIP+ INs during social preference did not result in apparent behavioral effects while the neurons were inhibited, but rather after the release of inhibition. Similarly, the behavioral effects of aIC VIP+ IN silencing during CS/US associations were not observed during fear acquisition but upon fear retrieval. Thus, our results point to a regulation of adaptive behaviors by aIC VIP+ INs involving cognitive processes. We cannot thus exclude that other neuronal types within the aIC might have been directly or indirectly affected by the inhibition of VIP+ IN activity and consequently implicated in the observed behavioral consequences. Future studies are warranted to dissect the mechanisms by which VIP+ INs influence circuit function in the aIC to modulate behavioral adaptations to sensory stimuli with behavioral relevance.

STAR★METHODS

Detailed methods are provided in the online version of this paper and include the following:

- KEY RESOURCES TABLE
- RESOURCE AVAILABILITY
  - Lead contact
  - Materials availability
  - Data and code availability
- EXPERIMENTAL MODEL AND SUBJECT DETAILS
- METHOD DETAILS
  - Surgical procedures
  - Deep-brain Ca^{2+} imaging
  - Optogenetic manipulation of behavior
  - Histology
- QUANTIFICATION AND STATISTICAL ANALYSIS
  - Ca^{2+} data analysis
  - Population vector analysis
  - Statistical analysis
  - Sample sizes, data exclusions and replication

SUPPLEMENTAL INFORMATION

Supplemental information can be found online at https://doi.org/10.1016/j.celrep.2022.110893.

ACKNOWLEDGMENTS

The authors thank all members of the Ferraguti lab for helpful discussions and comments, and Gabi Schmid and Sabine Schönherr for excellent technical assistance. They also thank Maria Sol Fustiñana, Claudia Schmuckermair, and Biafra Ahanonu for providing advice on deep-brain Ca^{2+} imaging data analyses, and Miodrag Mitric for helping with the setup of optogenetics experiments. The authors are grateful to E. Boyden, K. Deisseroth, D. Kim, I. Wickersham, J. Naughton, E. Callaway, and The Vector Core at the University of North Carolina at Chapel Hill (UNC Vector Core) for viral constructs. The authors also thank Helena Ariño for providing scientific illustrations. This work was supported by the Austrian Science Fund grants F44-17-B23 and W012060-10 to F.F. and the Eurolife consortium fellowship to M.Y.M.

AUTHOR CONTRIBUTIONS

Conceptualization, A.R.-P., E.P., and F.F.; software, A.R.-P. and M.S.; validation, A.R.-P. and F.C.; formal analysis, A.R.-P., E.P., F.C., F.F., H.H., and M.Y.M.; investigation, A.R.-P., E.P., and F.C.; writing – original draft, A.R.-P., E:P., and F.F.; writing – review & editing, A.R.-P., E.P., F.F., and M.S.; visualization, A.R.-P., E.P., F.C., and F.F.; supervision, F.F., E.P., and G.G.; funding acquisition, F.F.

DECLARATION OF INTERESTS

The authors declare no competing interests.

Received: May 20, 2021
Revised: January 20, 2022
Accepted: May 9, 2022
Published: May 31, 2022

REFERENCES

Alvarez, R.P., Kirlic, N., Misaki, M., Bodurka, J., Rhudy, J.L., Paulus, M.P., and Drevets, W.C. (2015). Increased anterior insula activity in anxious individuals is linked to diminished perceived control. Transl. Psychiatry *5*, E591. https://doi.org/10.1038/tp.2015.84.

Anastasiades, P.G., Collins, D.P., and Carter, A.G. (2021). Mediodorsal and ventromedial thalamus engage distinct L1 circuits in the prefrontal cortex. Neuron *109*, 314–330.e4. https://doi.org/10.1016/j.neuron.2020.10.031E4.

Ayzenshtat, I., Karnani, M.M., Jackson, J., and Yuste, R. (2016). Cortical control of spatial resolution by VIP $^{+}$ interneurons. J. Neurosci. *36*, 11498–11509. https://doi.org/10.1523/jneurosci.1920-16.2016.

Bariselli, S., Tzanoulinou, S., Glangetas, C., Prévost-Solié, C., Pucci, L., Viguié, J., Bezzi, P., O'connor, E.C., Georges, F., Lüscher, C., and Bellone, C. (2016). Shank3 controls maturation of social reward circuits in the vta. Nat. Neurosci. *19*, 926–934. https://doi.org/10.1038/nn.4319.

Batista-Brito, R., Vinck, M., Ferguson, K.A., Chang, J.T., Laubender, D., Lur, G., Mossner, J.M., Hernandez, V.G., Ramakrishnan, C., Deisseroth, K., et al. (2017). Developmental dysfunction of vip interneurons impairs cortical circuits. Neuron *95*, 884–895. https://doi.org/10.1016/j.neuron.2017.07.034.

Beer, A.L., Plank, T., Meyer, G., and Greenlee, M.W. (2013). Combined diffusion-weighted and functional magnetic resonance imaging reveals A temporal-occipital network involved in auditory-visual object processing. Front. Integr. Neurosci. *7*, 5. https://doi.org/10.3389/fnint.2013.00005.

Carta, I., Chen, C.H., Schott, A.L., Dorizan, S., and Khodakhah, K. (2019). Cerebellar modulation of the reward circuitry and social behavior. Science *363*, Eaav0581. https://doi.org/10.1126/science.aav0581.

Cone, J.J., Scantlen, M.D., Histed, M.H., and Maunsell, J.H.R. (2019). Different inhibitory interneuron cell classes make distinct contributions to visual contrast perception. Eneuro *6*, ENEURO.0337-18. https://doi.org/10.1523/eneuro.0337-18.2019.

Connor, J.R., and Peters, A. (1984). Vasoactive intestinal polypeptide-immunoreactive neurons in rat visual cortex. Neuroscience *12*, 1027–1044. https://doi.org/10.1016/0306-4522(84)90002-2.

Corbetta, M., Patel, G., and Shulman, G.L. (2008). The reorienting system of the human brain: from environment to theory of mind. Neuron *58*, 306–324. https://doi.org/10.1016/j.neuron.2008.04.017.

Corder, G., Ahanonu, B., Grewe, B.F., Wang, D., Schnitzer, M.J., and Scherrer, G. (2019). An amygdalar neural ensemble that encodes the unpleasantness of pain. Science *363*, 276–281. https://doi.org/10.1126/science.aap8586.

Di Martino, A., Shehzad, Z., Kelly, C., Roy, A.K., Gee, D.G., Uddin, L.Q., Gotimer, K., Klein, D.F., Castellanos, F.X., and Milham, M.P. (2009). Relationship between cingulo-insular functional connectivity and autistic traits in

neurotypical adults. Am. J. Psychiatry *166*, 891–899. https://doi.org/10.1176/appi.ajp.2009.08121894.

Downar, J., Crawley, A.P., Mikulis, D.J., and Davis, K.D. (2001). The effect of task relevance on the cortical response to changes in visual and auditory stimuli: an event-related fmri study. Neuroimage *14*, 1256–1267. https://doi.org/10.1006/nimg.2001.0946.

Downar, J., Crawley, A.P., Mikulis, D.J., and Davis, K.D. (2002). A cortical network sensitive to stimulus salience in A neutral behavioral context across multiple sensory modalities. J. Neurophysiol. *87*, 615–620. https://doi.org/10.1152/jn.00636.2001.

Ferguson, B.R., and Gao, W.J. (2018). Thalamic control of cognition and social behavior via regulation of gamma-aminobutyric acidergic signaling and excitation/inhibition balance in the medial prefrontal cortex. Biol. Psychiatry *83*, 657–669. https://doi.org/10.1016/j.biopsych.2017.11.033.

Ferguson, K.A., and Cardin, J.A. (2020). Mechanisms underlying gain modulation in the cortex. Nat. Rev. Neurosci. *21*, 80–92. https://doi.org/10.1038/s41583-019-0253-y.

Ferraguti, et al. (2004). Immunolocalization of metabotropic glutamate receptor 1α (mGluR1α) in distinct classes of interneuron in the CA1 region of the rat hippocampus. Hippocampus *14*. https://doi.org/10.1002/hipo.10163.

Franklin, K.B.J. (2008). The Mouse Brain in Stereotaxic Coordinates/Keith B.J. Franklin, George Paxinos (Elsevier).

Friard, O., and Gamba, M. (2016). Boris: a free, versatile open-source event-logging software for video/audio coding and live observations. Methods Ecol. Evol. *7*, 1325–1330. https://doi.org/10.1111/2041-210x.12584.

Fu, Y., Tucciarone, J.M., Espinosa, J.S., Sheng, N., Darcy, D.P., Nicoll, R.A., Huang, Z.J., and Stryker, M.P. (2014). A cortical circuit for gain control by behavioral state. Cell *156*, 1139–1152. https://doi.org/10.1016/j.cell.2014.01.050.

Garrett, M., Manavi, S., Roll, K., Ollerenshaw, D.R., Groblewski, P.A., Ponvert, N.D., Kiggins, J.T., Casal, L., Mace, K., Williford, A., et al. (2020). Experience shapes activity dynamics and stimulus coding of vip inhibitory cells. Elife *9*. https://doi.org/10.7554/elife.50340.

Gehrlach, D.A., Dolensek, N., Klein, A.S., Roy Chowdhury, R., Matthys, A., Junghänel, M., Gaitanos, T.N., Podgornik, A., Black, T.D., Reddy Vaka, N., et al. (2019). Aversive state processing in the posterior insular cortex. Nat. Neurosci. *22*, 1424–1437. https://doi.org/10.1038/s41593-019-0469-1.

Gehrlach, D.A., Weiand, C., Gaitanos, T.N., Cho, E., Klein, A.S., Hennrich, A.A., Conzelmann, K.K., and Gogolla, N. (2020). A whole-brain connectivity map of mouse insular cortex. Elife *9*. https://doi.org/10.7554/elife.55585.

Ghosh, K.K., Burns, L.D., Cocker, E.D., Nimmerjahn, A., Ziv, Y., Gamal, A.E., and Schnitzer, M.J. (2011). Miniaturized integration of A fluorescence microscope. Nat. Methods *8*, 871–878. https://doi.org/10.1038/nmeth.1694.

Goff, K.M., and Goldberg, E.M. (2019). Vasoactive intestinal peptide-expressing interneurons are impaired in A mouse model of Dravet syndrome. Elife *8*. https://doi.org/10.7554/elife.46846.

Gogolla, N. (2017). The insular cortex. Curr. Biol. *27*, R580–R586. https://doi.org/10.1016/j.cub.2017.05.010.

Grewe, B.F., Gründemann, J., Kitch, L.J., Lecoq, J.A., Parker, J.G., Marshall, J.D., Larkin, M.C., Jercog, P.E., Grenier, F., Li, J.Z., et al. (2017). Neural ensemble dynamics underlying A long-term associative memory. Nature *543*, 670–675. https://doi.org/10.1038/nature21682.

Guet-Mccreight, A., Skinner, F.K., and Topolnik, L. (2020). Common principles in functional organization of vip/calretinin cell-driven disinhibitory circuits across cortical areas. Front. Neural Circuits *14*. https://doi.org/10.3389/fncir.2020.00032.

Hangya, B., Ranade, S.P., Lorenc, M., and Kepecs, A. (2015). Central cholinergic neurons are rapidly recruited by reinforcement feedback. Cell *162*, 1155–1168. https://doi.org/10.1016/j.cell.2015.07.057.

He, M., Tucciarone, J., Lee, S., Nigro, M.J., Kim, Y., Levine, J.M., Kelly, S.M., Krugikov, I., Wu, P., Chen, Y., et al. (2016). Strategies and tools for combinatorial targeting of gabaergic neurons in mouse cerebral cortex. Neuron *91*, 1228–1243. https://doi.org/10.1016/j.neuron.2016.08.021.

Henson, R.N., and Rugg, M.D. (2003). Neural response suppression, haemodynamic repetition effects, and behavioural priming. Neuropsychologia *41*, 263–270. https://doi.org/10.1016/s0028-3932(02)00159-8.

Hersman, S., Allen, D., Hashimoto, M., Brito, S.I., and Anthony, T.E. (2020). Stimulus salience determines defensive behaviors elicited by aversively conditioned serial compound auditory stimuli. Elife *9*. https://doi.org/10.7554/elife.53803.

Holland, P.C. (1980). Influence of visual conditioned stimulus characteristics on the form of pavlovian appetitive conditioned responding in rats. J. Exp. Psychol. Anim. Behav. Process. *6*, 81–97. https://doi.org/10.1037/0097-7403.6.1.81.

Ishai, A., Pessoa, L., Bikle, P.C., and Ungerleider, L.G. (2004). Repetition suppression of faces is modulated by emotion. Proc. Natl. Acad. Sci. U S A *101*, 9827–9832. https://doi.org/10.1073/pnas.0403559101.

Kapur, S. (2003). Psychosis as A state of aberrant salience: a framework linking biology, phenomenology, and pharmacology in schizophrenia. Am. J. Psychiatry *160*, 13–23. https://doi.org/10.1176/appi.ajp.160.1.13.

Kastli, R., Vighagen, R., Van Der Bourg, A., Argunsah, A.Ö., Iqbal, A., Voigt, F.F., Kirschenbaum, D., Aguzzi, A., Helmchen, F., and Karayannis, T. (2020). Developmental divergence of sensory stimulus representation in cortical interneurons. Nat. Commun. *11*, 5729. https://doi.org/10.1038/s41467-020-19427-z.

Keller, A.J., Dipoppa, M., Roth, M.M., Caudill, M.S., Ingrosso, A., Miller, K.D., and Scanziani, M. (2020). A disinhibitory circuit for contextual modulation in primary visual cortex. Neuron *108*, 1181–1193.e8. https://doi.org/10.1016/j.neuron.2020.11.013.

Kim, H., Ährlund-Richter, S., Wang, X., Deisseroth, K., and Carlén, M. (2016). Prefrontal parvalbumin neurons in control of attention. Cell *164*, 208–218. https://doi.org/10.1016/j.cell.2015.11.038.

Kim, I.H., Kim, N., Kim, S., Toda, K., Catavero, C.M., Courtland, J.L., Yin, H.H., and Soderling, S.H. (2020). Dysregulation of the synaptic cytoskeleton in the pfc drives neural circuit pathology, leading to social dysfunction. Cell Rep. *32*, 107965. https://doi.org/10.1016/j.celrep.2020.107965.

Krabbe, S., Gründemann, J., and Lüthi, A. (2018). Amygdala inhibitory circuits regulate associative fear conditioning. Biol. Psychiatry *83*, 800–809. https://doi.org/10.1016/j.biopsych.2017.10.006.

Krabbe, S., Paradiso, E., D'aquin, S., Bitterman, Y., Courtin, J., Xu, C., Yonehara, K., Markovic, M., Müller, C., Eichlisberger, T., et al. (2019). Adaptive disinhibitory gating by vip interneurons permits associative learning. Nat. Neurosci. *22*, 1834–1843. https://doi.org/10.1038/s41593-019-0508-y.

Kuchibhotla, K.V., Gill, J.V., Lindsay, G.W., Papadoyannis, E.S., Field, R.E., Sten, T.A.H., Miller, K.D., and Froemke, R.C. (2017). Parallel processing by cortical inhibition enables context-dependent behavior. Nat. Neurosci. *20*, 62–71. https://doi.org/10.1038/nn.4436.

Kvitsiani, D., Ranade, S., Hangya, B., Taniguchi, H., Huang, J.Z., and Kepecs, A. (2013). Distinct behavioural and network correlates of two interneuron types in prefrontal cortex. Nature *498*, 363–366. https://doi.org/10.1038/nature12176.

Lamm, C., and Singer, T. (2010). The role of anterior insular cortex in social emotions. Brain Struct. Funct. *214*, 579–591. https://doi.org/10.1007/s00429-010-0251-3.

Lavin, T.K., Jin, L., Lea, N.E., and Wickersham, I.R. (2020). Monosynaptic tracing success depends critically on helper virus concentrations. Front Synaptic Neurosci. *12*, 6. https://doi.org/10.3389/fnsyn.2020.00006.

Lee, A.T., Cunniff, M.M., See, J.Z., Wilke, S.A., Luongo, F.J., Ellwood, I.T., Ponnavolu, S., and Sohal, V.S. (2019). Vip interneurons contribute to avoidance behavior by regulating information flow across hippocampal-prefrontal networks. Neuron *102*, 1223–1234.e4. https://doi.org/10.1016/j.neuron.2019.04.001.

Lee, S., Ahmed, T., Lee, S., Kim, H., Choi, S., Kim, D.-S., Kim, S.J., Cho, J., and Shin, H.-S. (2012). Bidirectional modulation of fear extinction by mediodorsal thalamic firing in mice. Nat. Neurosci. *15*, 308–314. https://doi.org/10.1038/nn.2999.

Letzkus, J.J., Wolff, S.B.E., Meyer, E.M.M., Tovote, P., Courtin, J., Herry, C., and Lüthi, A. (2011). A disinhibitory microcircuit for associative fear learning in the auditory cortex. Nature *480*, 331–335. https://doi.org/10.1038/nature10674.

Lin, S.C., and Nicolelis, M.A. (2008). Neuronal ensemble bursting in the basal forebrain encodes salience irrespective of valence. Neuron *59*, 138–149. https://doi.org/10.1016/j.neuron.2008.04.031.

Lissek, S. (2012). Toward an account of clinical anxiety predicated on basic, neurally mapped mechanisms of pavlovian fear-learning: the case for conditioned overgeneralization. Depress. Anxiety *29*, 257–263. https://doi.org/10.1002/da.21922.

Liu, K., Kim, J., Kim, D.W., Zhang, Y.S., Bao, H., Denaxa, M., Lim, S.A., Kim, E., Liu, C., Wickersham, I.R., et al. (2017). Lhx6-Positive gaba-releasing neurons of the zona incerta promote sleep. Nature *548*, 582–587. https://doi.org/10.1038/nature23663.

Livneh, Y., and Andermann, M.L. (2021). Cellular activity in insular cortex across seconds to hours: sensations and predictions of bodily states. Neuron *109*, 3576–3593. https://doi.org/10.1016/j.neuron.2021.08.036.

Ma, G., Liu, Y., Wang, L., Xiao, Z., Song, K., Wang, Y., Peng, W., Liu, X., Wang, Z., Jin, S., et al. (2021). Hierarchy in sensory processing reflected by innervation balance on cortical interneurons. Sci. Adv. *7*, Eabf5676. https://doi.org/10.1126/sciadv.abf5676.

Menon, V. (2015). Salience network. In Brain Mapping, A.W. Toga, ed. (Academic Press).

Mesik, L., Ma, W.-P., Li, L.-Y., Ibrahim, L.A., Huang, Z.J., Zhang, L.I., and Tao, H.W. (2015). Functional response properties of vip-expressing inhibitory neurons in mouse visual and auditory cortex. Front. Neural Circuits *09*. https://doi.org/10.3389/fncir.2015.00022.

Miura, I., Sato, M., Overton, E.T.N., Kunori, N., Nakai, J., Kawamata, T., Nakai, N., and Takumi, T. (2020). Encoding of social exploration by neural ensembles in the insular cortex. PLoS Biol. *18*, E3000584. https://doi.org/10.1371/journal.pbio.3000584.

Mossner, J.M., Batista-Brito, R., Pant, R., and Cardin, J.A. (2020). Developmental loss of Mecp2 from vip interneurons impairs cortical function and behavior. Elife *9*. https://doi.org/10.7554/elife.55639.

Mukamel, E.A., Nimmerjahn, A., and Schnitzer, M.J. (2009). Automated analysis of cellular signals from large-scale calcium imaging data. Neuron *63*, 747–760. https://doi.org/10.1016/j.neuron.2009.08.009.

Nadler, J.J., Moy, S.S., Dold, G., Trang, D., Simmons, N., Perez, A., Young, N.B., Barbaro, R.P., Piven, J., Magnuson, T.R., and Crawley, J.N. (2004). Automated apparatus for quantitation of social approach behaviors in mice. Genes Brain Behav. *3*, 303–314. https://doi.org/10.1111/j.1601-183x.2004.00071.x.

Naskar, S., Qi, J., Pereira, F., Gerfen, C.R., and Lee, S. (2021). Cell-type-specific recruitment of gabaergic interneurons in the primary somatosensory cortex by long-range inputs. Cell Rep. *34*, 108774. https://doi.org/10.1016/j.celrep.2021.108774.

Nobre, A.C., and Van Ede, F. (2018). Anticipated moments: temporal structure in attention. Nat. Rev. Neurosci. *19*, 34–48. https://doi.org/10.1038/nrn.2017.141.

Odriozola, P., Uddin, L.Q., Lynch, C.J., Kochalka, J., Chen, T., and Menon, V. (2016). Insula response and connectivity during social and non-social attention in children with autism. Soc. Cogn. Affect Neurosci. *11*, 433–444. https://doi.org/10.1093/scan/nsv126.

Pakan, J.M., Lowe, S.C., Dylda, E., Keemink, S.W., Currie, S.P., Coutts, C.A., and Rochefort, N.L. (2016). Behavioral-state modulation of inhibition is context-dependent and cell type specific in mouse visual cortex. Elife *5*. https://doi.org/10.7554/elife.14985.

Pannekoek, J.N., Veer, I.M., Van Tol, M.J., Van Der Werff, S.J., Demenescu, L.R., Aleman, A., Veltman, D.J., Zitman, F.G., Rombouts, S.A., and Van Der Wee, N.J. (2013). Resting-state functional connectivity abnormalities in limbic and salience networks in social anxiety disorder without comorbidity. Eur. Neuropsychopharmacol. *23*, 186–195. https://doi.org/10.1016/j.euroneuro.2012.04.018.

Pi, H.J., Hangya, B., Kvitsiani, D., Sanders, J.I., Huang, Z.J., and Kepecs, A. (2013). Cortical interneurons that specialize in disinhibitory control. Nature *503*, 521–524. https://doi.org/10.1038/nature12676.

Porter, J.T., Cauli, B., Staiger, J.F., Lambolez, B., Rossier, J., and Audinat, E. (1998). Properties of bipolar vipergic interneurons and their excitation by pyramidal neurons in the rat neocortex. Eur. J. Neurosci. *10*, 3617–3628. https://doi.org/10.1046/j.1460-9568.1998.00367.x.

Prönneke, A., Scheuer, B., Wagener, R.J., Möck, M., Witte, M., and Staiger, J.F. (2015). Characterizing vip neurons in the barrel cortex of vipcre/tdtomato mice reveals layer-specific differences. Cereb. Cortex *25*, 4854–4868. https://doi.org/10.1093/cercor/bhv202.

Ramos-Prats, A., Kölldorfer, J., Paolo, E., Zeidler, M., Schmid, G., and Ferraguti, F. (2019). An appraisal of the influence of the metabotropic glutamate 5 (Mglu5) receptor on sociability and anxiety. Front Mol. Neurosci. *12*, 30. https://doi.org/10.3389/fnmol.2019.00030.

Remedios, R., Kennedy, A., Zelikowsky, M., Grewe, B.F., Schnitzer, M.J., and Anderson, D.J. (2017). Social behaviour shapes hypothalamic neural ensemble representations of conspecific sex. Nature *550*, 388–392. https://doi.org/10.1038/nature23885.

Rhomberg, T., Rovira-Esteban, L., Vikór, A., Paradiso, E., Kremser, C., Nagy-Pál, P., Papp, O.I., Tasan, R., Erdélyi, F., Szabó, G., et al. (2018). Vasoactive intestinal polypeptide-immunoreactive interneurons within circuits of the mouse basolateral amygdala. J. Neurosci. *38*, 6983–7003. https://doi.org/10.1523/jneurosci.2063-17.2018.

Seeley, W.W., Menon, V., Schatzberg, A.F., Keller, J., Glover, G.H., Kenna, H., Reiss, A.L., and Greicius, M.D. (2007). Dissociable intrinsic connectivity networks for salience processing and executive control. J. Neurosci. *27*, 2349–2356. https://doi.org/10.1523/jneurosci.5587-06.2007.

Sforazzini, F., Schwarz, A.J., Galbusera, A., Bifone, A., and Gozzi, A. (2014). Distributed bold and cbv-weighted resting-state networks in the mouse brain. Neuroimage *87*, 403–415. https://doi.org/10.1016/j.neuroimage.2013.09.050.

Shi, T., Feng, S., Wei, M., and Zhou, W. (2020). Role of the anterior agranular insular cortex in the modulation of fear and anxiety. Brain Res. Bull *155*, 174–183. https://doi.org/10.1016/j.brainresbull.2019.12.003.

Sreepathi, et al. (2012). Subpopulations of neurokinin 1 receptor-expressing neurons in the rat lateral amygdala display a differential pattern of innervation from distinct glutamatergic afferents. Neuroscience *203*. https://doi.org/10.1016/j.neuroscience.2011.12.006.

Sunkin, S.M., Ng, L., Lau, C., Dolbeare, T., Gilbert, T.L., Thompson, C.L., Hawrylycz, M., and Dang, C. (2013). Allen brain atlas: an integrated spatio-temporal portal for exploring the central nervous system. Nucleic Acids Res. *41*, D996–D1008. https://doi.org/10.1093/nar/gks1042.

Terasawa, Y., Shibata, M., Moriguchi, Y., and Umeda, S. (2013). Anterior insular cortex mediates bodily sensibility and social anxiety. Soc. Cogn. Affective Neurosci. *8*, 259–266. https://doi.org/10.1093/scan/nss108.

Thévenaz, P., Ruttimann, U.E., and Unser, M. (1998). A pyramid approach to subpixel registration based on intensity. Ieee Trans. Image Process. *7*, 27–41. https://doi.org/10.1109/83.650848.

Turi, G.F., Li, W.K., Chavlis, S., Pandi, I., O'hare, J., Priestley, J.B., Grosmark, A.D., Liao, Z., Ladow, M., Zhang, J.F., et al. (2019). Vasoactive intestinal polypeptide-expressing interneurons in the Hippocampus support goal-oriented spatial learning. Neuron *101*, 1150–1165.e8. https://doi.org/10.1016/j.neuron.2019.01.009.

Uddin, L.Q. (2015). Salience processing and insular cortical function and dysfunction. Nat. Rev. Neurosci. *16*, 55–61. https://doi.org/10.1038/nrn3857.

Uddin, L.Q., and Menon, V. (2009). The anterior insula in autism: under-connected and under-examined. Neurosci. Biobehav Rev. *33*, 1198–1203. https://doi.org/10.1016/j.neubiorev.2009.06.002.

Uddin, L.Q., Nomi, J.S., Hébert-Seropian, B., Ghaziri, J., and Boucher, O. (2017). Structure and function of the human insula. J. Clin. Neurophysiol. *34*, 300–306. https://doi.org/10.1097/WNP.0000000000000377.

Uddin, L.Q., Supekar, K., Lynch, C.J., Khouzam, A., Phillips, J., Feinstein, C., Ryali, S., and Menon, V. (2013). Salience network–based classification and

prediction of symptom severity in children with autism. JAMA Psychiatry *70*, 869–879. https://doi.org/10.1001/jamapsychiatry.2013.104.

Walker, F., Möck, M., Feyerabend, M., Guy, J., Wagener, R.J., Schubert, D., Staiger, J.F., and Witte, M. (2016). Parvalbumin- and vasoactive intestinal polypeptide-expressing neocortical interneurons impose differential inhibition on martinotti cells. Nat. Commun. *7*, 13664. https://doi.org/10.1038/ncomms13664.

Wu, Y., Chen, C., Chen, M., Qian, K., Lv, X., Wang, H., Jiang, L., Yu, L., Zhuo, M., and Qiu, S. (2020). The anterior insular cortex unilaterally controls feeding in response to aversive visceral stimuli in mice. Nat. Commun. *11*, 640. https://doi.org/10.1038/s41467-020-14281-5.

Wylie, K.P., and Tregellas, J.R. (2010). The role of the insula in schizophrenia. Schizophr Res. *123*, 93–104. https://doi.org/10.1016/j.schres.2010.08.027.

Zhou, K., Zhu, L., Hou, G., Chen, X., Chen, B., Yang, C., and Zhu, Y. (2021). The contribution of thalamic nuclei in salience processing. Front. Behav. Neurosci. *15*. https://doi.org/10.3389/fnbeh.2021.634618.

Zhou, T., Zhu, H., Fan, Z., Wang, F., Chen, Y., Liang, H., Yang, Z., Zhang, L., Lin, L., Zhan, Y., et al. (2017). History of winning remodels thalamo-pfc circuit to reinforce social dominance. Science *357*, 162–168. https://doi.org/10.1126/science.aak9726.

Zweynert, S., Pade, J.P., Wüstenberg, T., Sterzer, P., Walter, H., Seidenbecher, C., Richardson-Klavehn, A., Düzel, E., and Schott, B. (2011). Motivational salience modulates hippocampal repetition suppression and functional connectivity in humans. Front. Hum. Neurosci. *5*. https://doi.org/10.3389/fnhum.2011.00144.

STAR★METHODS

KEY RESOURCES TABLE

REAGENT or RESOURCE	SOURCE	IDENTIFIER
Antibodies		
VIP-rabbit	Immunostar	lot: 1744002; RRID:AB_572270
RFP-mouse	Rockland	lot: 37699; RRID:AB_2611063
GFP-goat	Frontiers Institute	lot: 2571574; RRID:AB_2571574
Bacterial and virus strains		
AAV2/1.syn.FLEX.splitTVA-EGFP-tTA	Addgene	#100798
AAV2/1.TREtight.mTagBFP2-B19G	Addgene	#100799
RV.EnvA.dG.mCherry	In house production	Batch 1
AAV2/5.CAG.flex.ArchT-GFP	UNC vector core	https://www.med.unc.edu/genetherapy/vectorcore/
AAV2/5.CAG.flex.GFP	UNC vector core	https://www.med.unc.edu/genetherapy/vectorcore/
AAV2/5.CamKIIa-hChR2(HI34R)-mCherry	Addgene	#26975
AAV2/9.CAG.flex.GCaMP6s	Addgene	#100842
Experimental models: Organisms/strains		
VIP-ires-cre mice	Jackson Laboratory	RRID:IMSR_JAX:010908
Ai9-tdTomato mice	Jackson Laboratory	RRID:IMSR_JAX:007909
Software and algorithms		
MATLAB	MathWorks	https://www.mathworks.com/products/matlab
Ca^{2+} imaging processing pipeline	GitHub	https://github.com/bahanonu/calciumImagingAnalysis
ANY-maze	ANY-maze	https://www.anymaze.co.uk
GraphPad	GraphPad Prism	https://www.graphpad.com
Python	Python Software Foundation	https://www.python.org
Boris	BORIS	http://www.boris.unito.it/
Original code	This Publication	https://doi.org/10.5281/zenodo.6477827

RESOURCE AVAILABILITY

Lead contact

Further information and requests for resources and reagents should be directed to and will be fulfilled by the Lead Contact, Francesco Ferraguti (Francesco.Ferraguti@i-.med.ac.at).

Materials availability

This study did not generate new unique reagents.

Data and code availability

- The data reported in this paper will be shared from the lead contact upon request.
- All original codes have been deposited at Zenodo and is publicly available as of the date of publication. The DOI is listed in the key resources table.
- Any additional information required to reanalyze the data reported in this paper is available from the lead contact upon request.

EXPERIMENTAL MODEL AND SUBJECT DETAILS

All animal procedures were performed according to institutional guidelines and were approved by the Austrian Animal Experimentation Ethics Board (animal license numbers 2020–0.602.380, BMWFW-66.011/0123-WF/V/3b/2017) and in compliance with the

European convention for the protection of vertebrate animals used for experimental and other scientific purposes, Animal Experiments Act 2012 (TVG 2012) and the EU Directive 2010/63/EU. Every effort was taken to minimize animal suffering and the number of animals used. Male heterozygous VIP-ires-cre mice (STOCK Viptm1(cre)Zjh/J; The Jackson Laboratory; RRID: IMSR_JAX:010908) were used for all experiments. For VIP co-localization studies only, VIP-ires-cre homozygous mice were crossed with Ai9-tdTomato mice (B6.Cg-Gt(ROSA)$^{26Sortm9(CAG-tdTomato)Hze}$/J; The Jackson Laboratory; RRID:IMSR_JAX: 007909) to generate VIP-cre::Ai9 double heterozygous mice. For behavioral and tracing experiments, only VIP-ires-cre adult male mice (aged 2–4 months at the time of injection) were used. Mice were individually housed for at least 3 weeks before starting behavioral experiments. All optogenetic experiments were performed by an experimenter blind to the treatment group, and littermates of the same sex were randomly assigned to the experimental groups. Animals were kept in a temperature-controlled room with a 12/12 h light/dark cycle with access to food and water ad libitum. All behavioral experiments were conducted during the light cycle.

METHOD DETAILS

Surgical procedures

Anesthesia was induced with a combination of intraperitoneally injected Ketamine (80 mg/kg; Ketasol, AniMedica) and Xylazine (5 mg/kg; Xylasol, Animedica) and maintained with 2% Sevofluran (SEVOrane). The head was then fixed on a stereotactic frame (Model 1900; Kopf Instruments) and ophthalmic ointment was applied to the eyes to avoid drying. Postoperative pain medication included administration of meloxicam (Metacam, Boehringer Ingelheim; 1 mg/kg subcutaneously).

At the end of the experimental procedures, mice were deeply anesthetized with thiopental sodium (150 mg/kg, i.p.) and transcardially perfused with a fixative made of 4% paraformaldehyde, 15% picric acid in 0.1 M phosphate-buffer (PB), pH 7.2–7.4. Brains were cut into 50 μm thick coronal sections using a vibratome (Leica Microsystems VT1000S, Vienna, Austria).

Mono-trans-synaptic rabies tracing

VIP-ires-cre mice (N = 7) were unilaterally injected with a 1:1 mixture of AAV1.syn.FLEX.splitTVA-EGFP-tTA (1.7 × 10^13 GC/mL, diluted 1:50, Addgene #100798) and AAV1.TREtight.mTagBFP2-B19G (3.2 × 10^13 GC/mL, Addgene #100799) into the aIC (coordinates from bregma: AP: +2.00 mm; ML: ± 2.75 mm; DV: 3.4 mm) in a volume of 300 nL. Mice were allowed to recover for 1 week before the injection of the rabies virus RV.EnvA.dG.mCherry (300 nL, produced in house; Viral Vector Core, Salk Institute) using the same coordinates. One week following the RV injection in the aIC, mice were transcardially perfused as described above.

Anterograde tracing

VIP-ires-cre mice (N = 2) were unilaterally injected with a AAV5.CamKIIa-hChR2(H134R)-mCherry (5.1 × 10^12 GC/mL, Addgene #26975) into the MD (coordinates from bregma: AP: −1.58mm; ML: +0.44 mm; DV: −3.20 mm) in a volume of 300 nL. Mice were allowed to recover for 3 weeks before perfusion to ensure adequate viral transduction.

Deep-brain Ca^{2+} imaging

VIP-ires-cre mice (N = 7) were unilaterally injected with 300 nL AAV2/9.CAG.flex.GCaMP6s (Addgene, #100842) into the aIC using a glass pipette (tip diameter ~30 μm) connected to a Picospritzer III microinjection system (Parker Hannifin Corporation) at the following coordinates from bregma: anterior–posterior (AP): +1.95 mm; medio–lateral (ML): +2.85 mm; dorso–ventral (DV): 3.3 mm. Immediately after the AAV injection, a GRIN lens (0.6 × 7.3 mm GLP-0673, Inscopix) was lowered into the aIC as previously described using a custom-built lens holder, and fixed to the skull using ultraviolet light-curable glue (Loctite 4305, Henkel) and miniature screws (P.A. Precision Screws). Dental acrylic (Paladur, Heraeus) was used to seal the skull and attach a custom-made head bar for animal head fixation during the miniature microscope mounting procedure. Mice were allowed to recover for 1 week after surgery before checking for GCaMP6s expression.

Optogenetic manipulations

VIP-ires-cre mice (N = 45) were bilaterally injected with AAV2/5.CAG.flex.ArchT-GFP (University of North Carolina vector core, UNC) or AAV2/5.CAG.flex.GFP (University of North Carolina vector core, UNC) into the aIC (300 nL per hemisphere, coordinates from bregma: AP: +1.95 mm; ML: ± 2.85 mm; DV: 3.3 mm). Immediately after the AAV injection, mice were bilaterally implanted with custom-made optic fiber connectors (fiber numerical aperture 0.5, fiber inner core diameter 200 μm, length: 5mm; Thorlabs). Fiber tips were lowered 3 mm below the cortical surface using a custom-built holder. Implants were fixed to the skull using cyanoacrylate glue (Ultra Gel, Henkel) and miniature screws (P.A. Precision Screws). Dental acrylic was used to seal the skull. Mice were allowed to recover for a minimum of 4 weeks before behavioral testing to ensure adequate viral transduction.

Deep-brain Ca^{2+} imaging

Ca^{2+} imaging studies in freely moving mice were performed via the implanted GRIN lens using a miniaturized microscope (nVista, V3, nVista HD; Inscopix) as previously described (Ghosh et al., 2011). A base plate for the miniature microscope was glued to the dental acrylic implant at least 1 week before the start of behavioral experiments. During this time, mice were habituated to a brief head-fixation on a running wheel in a custom-made mounting station and to the miniature microscope attachment procedure. Images were acquired using the nVista HD software (Inscopix) at 1024 x 800 pixels, covering a field-of-view of approximately 600 μm × 600 μm , at a frame rate of 20 Hz. Imaging parameters were set at LED power of 40–80% (0.9–1.7 mW at the objective, 475 nm). For each mouse, the same parameters were maintained across repeated behavioral sessions. Time stamps of imaging

frames and behavioral stimuli were collected for alignment using the AMi-2 Digital interface (ANY-maze). All behavioral sessions were recorded using an overhead camera and the ANY-maze software.

Social preference test

Social preference was assessed by means of a modified classical three-chamber social task (Ramos-Prats et al., 2019), consisting of an empty rectangular arena (75 cm long × 30 cm wide × 35 cm tall) placed inside a sound-attenuating chamber under infrared illumination. The test mouse was allowed to habituate to the arena for 10 min. After this habituation period, it was guided to the center of the arena, and a novel unfamiliar mouse (juvenile 4–8 week old C57Bl6/J male mouse) was placed into a mesh enclosure in one corner, whereas an identical empty mesh enclosure was placed in the opposite corner of the arena. The mesh enclosure allowed for air exchange, visual, olfactory and auditory interaction, but prevented fighting and biting of the miniature microscope cable by the interactor mouse. The test mouse was then allowed to explore the chamber for 10 min. Behavioral measurements during this test phase included visits to the conspecific mouse or empty enclosure (object) (<10 cm, for a minimum of 5s) and overall time spent in proximity. The chamber and enclosures were cleaned before and between subjects with 70% ethanol. On test day 2, the same identical procedure was performed, with the position of the empty mesh enclosure and the one containing an unfamiliar interactor exchanged. Tracking was automatically performed using the ANY-maze software and analyzed with custom-written MATLAB (MathWorks) scripts.

Fear conditioning and memory retrieval

On testing day 1 (fear conditioning), mice were placed in a 30 × 30 cm chamber with transparent walls and a metal rod floor (context A) (Ugo Basile, Comerio, Italy) inside a sound-attenuating chamber under low light conditions. Behavioral protocols for stimuli control were generated using the ANY-maze software via TTL pulses.

Following a 240 s acclimation period, an 80 dB white noise [conditioned stimulus (CS)] lasting 30 s followed by a 2 s delivery of a 0.5 mA alternating current footshock [unconditioned stimulus (US)] was delivered five times with pseudorandom inter-trial interval (ITI) (range of 64–104 s). The chamber was cleaned before and between subjects with 70% ethanol. After twenty-four hours (testing day 2) mice were tested for fear memory retrieval. Animals were placed in a 30 x 30 chamber that differed from the conditioning context by having a solid Plexiglass floor and black and white stripes and squares patterns on the walls. Following a 240 s acclimation period, the same CS, lasting 30 s, was presented five times with a pseudorandom ITI (range of 60–100 s). The chamber was cleaned with 1% acetic acid before and between subjects. Mice were tracked using contour tracking and center of mass (ANY-maze). Automatic freezing assessment resulted inaccurate due to cable movements and thus freezing was manually scored by trained experimenters using frame-by-frame analysis with Boris (Friard and Gamba, 2016).

Auditory exposure test

Mice were head-fixed on a running wheel in a custom-made mounting station identical to the one used for microscope attachment procedure habituations and placed inside a sound-attenuating chamber under low light conditions, and with a background noise of 45 dB. Following a brief habituation after the miniaturized microscope attachment (1–2 min), mice were exposed to a protocol consisting of a set of two different tones (50 dB or 80 dB, 6 kHz) presented with pseudorandom ITI (range 3–24 s, ~10 s inter-tone ITI). All mice underwent the same protocol sequence of tone presentations and were placed at the same distance from the speaker. Tone presentations were triggered using the ANY-maze software via TTL pulses. The mounting station and running wheel were cleaned with 70% ethanol before and between subjects.

Optogenetic manipulation of behavior

Before behavioral experiments, all mice were handled for at least 3 days and habituated to the optical fiber attachment procedure. On experimental days, mice were tethered to optic patch cords (0.48 NA; Doric Lenses) and connected to a custom-built laser bench setup via a rotary joint (Doric Lenses). An acousto-optic tunable filter controlled the laser intensity (MGL-F-589, 589-nm wavelength). We used ANY-maze to track mice in real time for closed-loop manipulations and to trigger optogenetic manipulations on the basis of the mouse location or protocol timeline. At the beginning of each behavioral test, the laser power at the tip of the patch cables was measured and adjusted with an optical power meter (PM100D, ThorLabs) to an intensity of 15 mW. All behavioral sessions were recorded using an overhead camera and the ANY-maze software.

Social preference

The same behavioral protocol as described above for deep-brain Ca^{2+} imaging was used with minor modifications. Mice were first individually allowed to habituate to the arena for 10 min. After this habituation period, the test mouse was guided to the center of the arena, and a novel unfamiliar mouse (juvenile 4-8-week-old C57Bl6/J male mouse) was placed into a mesh enclosure in one corner whereas an identical empty mesh enclosure was placed in the opposite corner of the arena. The position of the empty and interactor enclosures was alternated and counterbalanced for each trial to avoid any location bias. The test mouse was then allowed to explore the chamber for 10 min, and was considered to be exploring the empty enclosure or the one containing the conspecific when the distance of the center of body mass was less than 10 cm away. We divided the test into two 5 min bins (Bariselli et al., 2016). For one set of experiments, the laser was turned on only during interaction periods with the enclosure containing the interactor mouse during the last 5 min of the test, while for the second set of experiments, the laser was turned on only during interactions within the first 5 min of the test. Similar to previous reports (Carta et al., 2019; Kim et al., 2020), the closed-loop optogenetic manipulation protocol during the social preference test led to bouts of laser stimulation that lasted on average 8.3 s, and ranged between 4.3 s and 14.8 s. Real-time tracking, to enable closed-loop optogenetic manipulations, was performed using an overhead camera and the AnyMaze

software. Measurements during this test phase included overall time spent in proximity (in s) to the conspecific mouse or empty enclosure (object). To determine the preference score for the social stimulus, we computed the social preference index based on interaction time (s) as follows: (mouse - object)/(mouse + object) *100. The chamber and enclosures were cleaned before and between subjects with 70% ethanol.

Real-time object place preference

This test was performed in a similar fashion as the social preference test described above. Briefly, each mouse was individually placed in a rectangular arena (75 cm long × 30 cm wide × 35 cm tall) placed inside a sound-attenuating chamber under infrared illumination. Following a 10 min habituation period, the test mouse was guided to the center of the arena, and two unfamiliar objects (lego blocks) were placed in opposite corners of the arena. Mice were considered to be exploring the objects when the distance of the center of body mass was less than 10 cm. Similar to the social preference test, the experiment was divided into two 5 min bins, and the laser was allowed to turn on only during the last 5 min of the test with one randomly assigned object. Measurements during this test phase included overall time spent in proximity to both objects. To determine the preference score for the inhibition-paired object, we computed the object preference index, based on interaction time (s) as follows: (object i - object)/(object i + object) *100, where object i corresponds to the randomly assigned object for paired closed-loop inhibition. The chamber and enclosures were cleaned before and between subjects with 70% ethanol.

Open field place preference

Similar to the real-time object place preference test, the experiment was divided into two 5 min bins, and the laser was allowed to turn on only during the last 5 min of the test in one randomly assigned quadrant (25 × 25cm) of the open field arena (50 × 50 × 30cm). Measurements during this test phase included time in each quadrant, general locomotion and locomotion in the inhibition-paired quadrant. The arena was cleaned before and between subjects with 70% ethanol.

Fear conditioning and retrieval

The same behavioral protocol as described above for deep-brain Ca^{2+} imaging was used with minor modifications. Light stimulation was delivered to ArchT- or GFP-injected mice during fear conditioning on day 1, for 4.5 s during the entire presentation of the 2 s US + stimulus (starting 500 msec before US onset) and extending for additional 2 s. On day 2, during the retrieval phase, mice were also tethered to the optic fibers, but underwent testing without optogenetic modulation. Mice were tracked using contour tracking and center of mass (ANY-maze). Freezing episodes were processed offline by trained experimenters using frame-by-frame analysis.

Histology

Quantification of VIP + INs

Immunocytochemistry experiments were carried out according to previously published procedures with minor modifications (Sreepathi, 2012). Free-floating sections were incubated in primary antibody solution [rabbit antibody against VIP (cat. no. 20077, Immunostar), diluted 1:4,000] containing 2% normal goat serum (NGS), 0.3% Triton X-100 (TX) in Tris-buffered saline (TBS-T; pH 7.4) for two days at 6°C and then in secondary antibody [biotinylated goat anti-rabbit (cat. no. BA-1000, Vector laboratories), diluted 1:500] overnight. After extensive washing, sections were incubated in an ABC complex solution (1:100, Vectastain ABC kit; Vector Laboratories) made up in TBS, followed by diaminobenzidine (DAB) as a chromogen (0.5 mg/mL in TB) and 0.003% H_2O_2, as the electron donor, for 5 min. The sections were mounted onto gelatin-coated slides, dehydrated in an ascending ethanol series followed by an incubation in butylacetate and coverslipped with Eukitt (Christine Gröpl, Tulln, Austria).

Sections immunolabeled for VIP were used to assess the number of VIP + INs (n = 4 mice) by an experienced experimenter using the Neurolucida software (MBF Bioscience). Borders of the IC were outlined with the help of consecutive Nissl stained sections and according to a mouse brain atlas (Franklin, 2008). While counting neurons, sections were focused throughout their whole thickness to obtain the most accurate quantification.

Immunofluorescence

Immunofluorescent experiments were performed according to previously published procedures (Ferraguti, 2004). Briefly, sections were first washed with TBS and then incubated in blocking solution made of 20% normal serum (as required) in 0.1% TBS-T, for 1 h at room temperature. After blocking, sections were incubated with primary antibodies (see Table S2) diluted in 2% normal serum and 0.2% TBS-T for 72 h at 6°C. Slices were then washed with TBS 3 times and then incubated overnight at 6°C with respective secondary antibody diluted in the same solution as used for the primary antibodies (see Table S2). Finally, sections were extensively washed with TBS, mounted on glass slides and coverslipped with Vectastain (Vector Laboratories) or ProLong Diamond (Thermo Fisher Scientific). Images were acquired using either an epifluorescence microscope (Axio Imager, Carl Zeiss, Oberkochen, Germany) and the Openlab software (Version 5.5.0) or an Airy Scan LSM980 laser scanning microscope (Carl Zeiss, Oberkochen, Germany) with a 40x/1.2 objective. Raw confocal images were channel dye separated and deconvolved using Huygens software (Scientific Volume Imaging, Hilversum, The Netherlands). Image processing was performed using the IMARIS 9.7.0 software (Oxford Instruments, Bitplane, Zurich, Switzerland).

To confirm the sensitivity of the VIP-IHC analysis, we carried out double fluorescence experiments using sections (2/animal; N = 3 mice) obtained from VIP-ires-cre:Ai9 mice. In these slices, we visualized the endogenous fluorescence of the reporter molecule tdTomato expressed under the endogenous VIP promoter and VIP using an immune-complex composed of a rabbit primary antibody (Immunostar), as described previously, and an Alexa 488-conjugated donkey anti-rabbit secondary antibody (cat. no. A21206, Invitrogen, 1:1,000). The sections were scanned using a LED Panoramic ® 250 Flash III scanner (3DHistech) equipped with a 16-bit

4.2 MP camera and a 20x objective, and the quantification of the neurons colocalizing the two fluorescent signals was manually performed offline using CaseViewer (3DHistech).

Image acquisition and data analysis

For mono-trans-synaptic tracing, brains were embedded in 2% agarose in PBS and cut into coronal sections. Every third section from each brain was used for quantification of first order presynaptic neurons to aIC VIP + INs. Four sections before and after the injection site were not used for quantification as they contained the starter cells. Whole slide imaging was performed with a 6 channel LED Panoramic ® 250 Flash III scanner (3DHistech) equipped with a 16-bit 4.2 MP camera and a 20x objective yielding a final resolution of 0.242 μm per pixel. 2-D images from the digital Allen Brain Atlas (Sunkin et al., 2013) were registered by means of linear local transformations to the coronal histological sections using a set of manually chosen landmarks (40 ± 10 per slice). Presynaptic neurons were quantified using a semi-automatic procedure. Briefly, labeled cells were automatically detected based on signal intensity and size and assigned to brain structures, as delineated in the reference atlas, according to their coordinates using a custom-written Python script. Subsequently, an expert experimenter, through visual inspection of the processed images, manually corrected for positive- and false-negative cells. Data are reported as cell counts normalized to the total cell counts per animal (percent of total input). Areas containing less than 1% of the total sum of inputs and the aIC itself were excluded.

Anatomical abbreviations of IC subdivisions used for figure display included: agranular insula (AI), agranular insular cortex, ventral (AIV), agranular insular cortex, dorsal (AID), dysgranular insular cortex (DI), granular insular cortex (GI), agranular insular cortex, posterior (AIP). Anatomical abbreviations of presynaptic brain areas used for figure display included: ventral orbital cortex (VO), lateral orbital cortex (LO), primary motor cortex (M1), dorsolateral orbital cortex (DLO), cecondary motor cortex (M2), piriform cortex (Pir), somatosensory cortex (SS), caudate putamen (CPu), globus pallidus (GP), ventral pallidum (VP), anterior amygdaloid area (AA), anterior cortical amygdaloid nucleus (ACo), basolateral amygdala (BLA), mediodorsal thalamic nucleus (MD), anteromedial thalamic nucleus (AM), submedius thalamic nucleus (Sub), perirhinal cortex (PRh), posterolateral cortical amygdaloid area (PLCo), posterior thalamic nuclei (Po), parafascicular thalamic nucleus (PaF), rubrospinal tract (RS), paraventricular thalamic nucleus (PV), intermediodorsal thalamic nucleus (IM), mediodorsal thalamic nucleus, central part (MDC), mediodorsal thalamic nucleus, medial part (MDM), mediodorsal thalamic nucleus, lateral part (MDL), ventrolateral thalamic nucleus (VL), central medial thalamic nucleus (CM), prelimbic cortex (PrL), claustrum (CL), medial orbital cortex (MO).

QUANTIFICATION AND STATISTICAL ANALYSIS

Ca^{2+} data analysis

Basic processing of Ca^{2+} imaging videos was performed using the MATLAB (MathWorks) pipeline developed by Corder and colleagues (Corder et al., 2019) available at https://github.com/bahanonu/calciumImagingAnalysis.

Briefly, imaging frames were first spatially down-sampled in both x and y lateral spatial dimensions using 4 × 4 bilinear interpolation. Following this, imaging frames were normalized by dividing each image by a spatially low-pass filtered version of the frame using a ImageJ software plugin. Next, X-Y movement was corrected using TurboReg (Thévenaz et al., 1998). After motion correction, each movie was temporally smoothed and down-sampled from 20 Hz to 5 Hz. Spatial filters for each individual neuron were defined using a semi-automated cell-sorting routine using principal and independent component analyses (Mukamel et al., 2009). We identified 11.9 ± 4.7 cells per mouse per day. Every cell included in the analysis was visually validated based on the spatial filter and activity trace. For activity analysis across pairs of different behavioral paradigms, we matched neurons across days by using a centroid-based alignment procedure (Corder et al., 2019). Relative changes in calcium fluorescence (F), were expressed as: $\Delta F(t)/F0 = (F(t) - F0)/F0$, where F0 is the mean image obtained by averaging the entire movie (Grewe et al., 2017; Remedios et al., 2017). Following this, activity traces were z-scored and linearly detrended to avoid possible influences of fluorescence decay during the imaging session. Stimulus responses were baselined to 2 s pre-interaction during social preference tests, 10 s pre-CS+ during fear conditioning and retrieval tests, and 1 s pre-tone presentation during auditory exposure testing. Stimulus response period was set to 30 s for CS, US, CS-R and US-, to 10 s for interactions during social preference testing, and to 3 s during tone presentations. The z-scored area under the curve (AUC) was used to assess the significance of activity responses during different stimuli presentations. To define responsive cells, average time-binned Ca^{2+} signals were compared between the stimulus presentation and equivalent baseline period, and classified as excited or inhibited ($\pm 2\sigma$ from baseline) during different stimuli presentations. To define coding neurons (CN), cells not displaying activity $\pm 2\sigma$ from baseline or displaying activity during all stimuli presentations during one specific session were defined as "other" (Remedios et al., 2017).

Population vector analysis

In order to compare the similarity of sets of classified groups of neurons (e.g., object vs mouse CN) response patterns, we measured the Mahalanobis distance between ensembles across time (Grewe et al., 2017). The dataset for each computation included two distributions of population activity vectors of N-dimensions (N = neurons) from the mean of all frames where a given pair of stimuli presentations occurred. Activity vectors were computed at different time points, using the minimum duration of a given stimulus across all imaged mice (e.g., maximum object interaction during day1 social interaction test) as the maximum time period considered for analysis. The Mahalanobis distance between sets of coding neurons was computed as:

$$M2 = (x - y)^T \bullet \sum^{-1} \bullet (x - \mu)$$

where x and μ are individual and mean population ensemble responses vectors, xT and μT their transposes and Σ the covariance matrix for a given set of ensemble responses.

Statistical analysis

We conducted all statistical analyses using GraphPad Prism (GraphPad Software, version 9) and MATLAB (MathWorks). Single-variable comparisons were made with two-tailed unpaired or paired t-tests or two-way repeated measures ANOVA followed up by post hoc tests in case of multiple-variable comparisons (as reported in figure legends and Table S1). Normality was checked with the Shapiro-Wilk criterion and, when violated, non-parametric statistics were performed. Correlation analyses were made using non-parametric linear regressions. Data are presented as mean ± SEM, and statistical significance levels are shown as exact p value or *$p < 0.05$, **$p < 0.01$ or ***$p < 0.001$ in all figures.

Sample sizes, data exclusions and replication

The size of our experimental samples was not pre-specified and was chosen to match or exceed those in previous studies related to our experimental designs (Krabbe et al., 2019; Bariselli et al., 2016). Reported n numbers refer to data from individual neurons while N is reported for number of mice. Data were collected from at least 6 mice (total of N = 71 neurons) for deep-brain Ca^{2+} imaging; from at least 7 mice for rabies tracings; from at least 11 mice per group and experiment for optogenetic manipulation of behavior. Only about 1/3 of mice implanted for deep-brain Ca^{2+} imaging showed detectable calcium signals and could be used for this study. Only one mouse used for deep-brain Ca^{2+} imaging was excluded *post hoc* from the social preference test on day 2 due to asynchronicity between calcium imaging data and behavioral performance. For rabies tracing and optogenetic experiments, animals were *post hoc* excluded from the analysis when optic fiber placement or viral expression resulted inaccurate (e.g., implant damage, not exhibiting correct fiber placement, weak virus expression). The following number of mice were excluded: ArchT, N = 4; GFP, N = 4; Rabies, N = 6. All experiments reported here were consistently reproduced in independent experimental groups for optogenetic behavioral manipulation or several mice for calcium imaging and rabies tracing experiments.